

# O VI, N V and C IV in the Galactic Halo: II. Velocity-Resolved Observations with Hubble and FUSE

Rémy Indebetouw<sup>1</sup> and J. Michael Shull<sup>2</sup>

*CASA, Dept. of Astrophysical and Planetary Sciences, University of Colorado, 389 UCB,  
Boulder, Colorado 80309-0389*

## ABSTRACT

We present a survey of N V and O VI (and where available C IV) in the Galactic halo, using data from the *Far Ultraviolet Spectroscopic Explorer* (FUSE) and the *Hubble Space Telescope* (HST) along 34 sightlines. These ions are usually produced in nonequilibrium processes such as shocks, evaporative interfaces, or rapidly cooling gas, and thus trace the dynamics of the interstellar medium. Searching for global trends in integrated and velocity-resolved column density ratios, we find large variations in most measures, with some evidence for a systematic trend of higher ionization (lower N V/O VI column density ratio) at larger positive line-of-sight velocities. The slopes of  $\log[N(\text{N V})/N(\text{O VI})]$  per unit velocity range from  $-0.015$  to  $+0.005$ , with a mean of  $-0.0032 \pm 0.0022(\text{r}) \pm 0.0014(\text{sys}) \text{ dex } (\text{km s}^{-1})^{-1}$ . We compare this dataset with models of velocity-resolved high-ion signatures of several common physical structures. The dispersion of the ratios, O VI/N V/C IV, supports the growing belief that no single model can account for hot halo gas, and in fact some models predict much stronger trends than are observed. It is important to understand the signatures of different physical structures to interpret specific lines of sight and future global surveys.

*Subject headings:* Galaxy: halo — ISM: structure — ultraviolet: ISM

---

<sup>1</sup>present address: Astronomy Department, University of Wisconsin, 475 N. Charter St, Madison, WI 53706 (remy@astro.wisc.edu)

<sup>2</sup>also at JILA, University of Colorado and National Institute of Standards and Technology (mshull@casa.colorado.edu)

## 1. Introduction

We are interested in understanding how the dynamics of the interstellar medium (ISM) of galaxies determines how the energy and matter released by stars are re-distributed. In a previous paper (Indebe-

touw & Shull 2004), hereafter denoted Paper I, we investigated theoretical models of the ionization ratios of Li-like absorbers, N V, O VI, C IV, in the Galactic halo. These ions are believed to form in nonequilibrium in shocks, evaporative interfaces, or rapidly cooling gas, all of which trace the dynamics of the interstellar medium. As a useful new diagnostic, in that paper we focused on *velocity-resolved* signatures of several common physical structures: (1) a cooling Galactic fountain flow that rises, cools, and recombines as it returns to the disk; (2) shocks moving toward the observer; (3) a conductive interface with the observer located in the hotter gas.

In this paper, we present a survey of 34 sightlines observed through the Galactic halo by the *Far Ultraviolet Spectroscopic Explorer* (FUSE) and the *Hubble Space Telescope* (HST) in the Li-like absorption lines of O VI, N V, and sometimes C IV. We report the integrated column densities of these three ions and their ratios. We also focus, as in Paper I, on the new, and potentially useful diagnostic provided by the velocity dependence of these ion ratios. The observable velocity-ionization trends are weak, because even strong trends are washed out by the large thermal width of the gas at different parts of the flow. Additional confusion results since the long sightlines almost definitely pass through multiple structures. We report an indication of a weak trend of decreasing  $N(\text{N V})/N(\text{O VI})$  at more positive velocities. The distribution of this slope is broad, with a mean value,  $-0.0032 \pm 0.0022(\text{r}) \pm 0.0014(\text{sys}) \text{ dex } (\text{km s}^{-1})^{-1}$ , displaced somewhat from zero.

In this paper, § 2 describes the data cal-

ibration and analysis. The basic observational results are described in § 3. Section 4 describes models of the dynamical signatures of the Li-like ions, and interpretation.

## 2. Observations and Data Reduction

We observe the relative distribution of Li-like ions in the interstellar medium using the FUSE satellite and the Space Telescope Imaging Spectrograph (STIS) and Goddard High Resolution Spectrograph (GHRS) on HST. The FUSE satellite consists of four coaligned Rowland circle spectrographs which redundantly cover the spectral range 910-1189 Å at  $R \sim 20,000$  resolution (Moos et al. 2000; Sahnou et al. 2000). The STIS instrument offers far-ultraviolet spectroscopy in first-order and echelle modes. Spectroscopic modes used in this study are the G140M first-order grating (55 Å in the range 1140-1740 Å,  $R \sim 15,000$ ) and the E140M echelle (1150-1710 Å,  $R \sim 50,000$ ) (Kimble et al. 1998; Davies et al. 2001). The GHRS was the precursor UV spectrograph to STIS on the HST, and offered similar capabilities without the imaging capability of STIS. Data used here were obtained with the G160M first-order grating (Brandt et al. 1994; Soderblom et al. 1995).

The data analysis consists of instrument-dependent calibration, followed by a common continuum and wavelength verification process. The corrections which are unique to a given bandpass are made (e.g., assessment of H<sub>2</sub> contamination which is only relevant to the O VI band), and finally the two or three bandpasses are combined to study the velocity-resolved C IV/N V/O VI column density ratios. Ta-

ble 1 shows the sightlines, with the instrument and dataset name for each (multi-exposure) observation, the total (nighttime for FUSE) exposure time, observation date, the principal investigator, and for HST instruments, the proposal ID number. All of the FUSE data are guaranteed time observations (GTO), and the GTO project can be identified by the first 3 numbers of the dataset name. STIS and GHRS first-order spectra only cover the C IV or the N V line; for those datasets the relevant ion is identified in the instrument column of the table. As described below, the GHRS wavelength scale can be improved using auxiliary datasets, and the ones used in this project are also listed.

## 2.1. Basic Calibration and Instrument-Specific Issues

### 2.1.1. Far Ultraviolet Spectroscopic Explorer

Most FUSE data issues are adequately resolved by the FUSE data pipeline (version 1.1 is described in Oegerle et al. 2000a, all data used here were re-reduced using version 1.8.7 and spot checked against 2.0.5). The pipeline screens for basic satellite location and orientation problems – South Atlantic Anomaly avoidance, earth avoidance, etc. (see Sembach et al. 2001b). Particular to FUSE are the thermal motions of the grating and telescope with orbital phase and spacecraft orientation with respect to the satellite orbit plane and the sun. Thermally induced grating motion is well understood and removed by the pipeline. Telescope motion is removed in the LiF1 channel because the spacecraft points using that optical path. A point source can move in the large aper-

tures of the second lithium fluoride channel LiF2 and both silicon carbide channels SiC1 and SiC2, and the spectral resolution and instrument throughput can be degraded. The detector characteristics are sufficiently different that it is inadvisable to directly combine data from different segments. Therefore, for O VI, the LiF1A segment are used for quantitative measurements, and the LiF2B data used for feature confirmation in cases of low signal-to-noise.

The FUSE data for each target were obtained from the archive in raw form, re-reduced and combined into single spectrum for each detector segment, with the following steps. A target may be observed several times, resulting in several *datasets*, each consisting of multiple *exposures*. All exposures were screened for bursts, and the remaining data were recalibrated using the FUSE pipeline (calibrated data was available from the archive but from earlier versions of the pipeline). The pipeline removes the time-dependent spectral motion from the grating motion and the orbital Doppler shift, removes detector background, extracts a 1-dimensional spectrum, and provides a flux calibration and wavelength solution. This recalibration also allows us to select only photons received during spacecraft night. Although not absolutely necessary for analysis of the O VI line in isolation, there are known artifacts in daytime data. For simplicity in this study, only nighttime data were used.

The FUSE pipeline wavelength solution at the time of this analysis was questionable, especially in its total offset (the relative scale is somewhat more trustworthy). For example, the heliocentric-to-LSR

conversion was applied with incorrect sign in v1.8.7. Multiple datasets were cross-correlated to find their relative wavelength offsets before combining, and the absolute wavelength scale was corrected using low-ionization interstellar lines as described below. Several datasets were recalibrated with v2.0.5, and no significant differences were found in the spectral region considered here, aside from the overall velocity offset, which had been corrected anyway.

### *2.1.2. Space Telescope Imaging Spectrograph*

STIS echelle data suffer from cross-order scatter, which degrades the spectral purity and increases the background in the extracted spectra. In fact, the standard STIS pipeline uses a linear interpolation of the count rate between orders to subtract the background when extracting a one-dimensional spectrum from the two-dimensional image. A better background algorithm, which models the two-dimensional scatter iteratively with the science spectrum, can be included in the STIS pipeline. All STIS echelle datasets were recalibrated through the pipeline with this additional algorithm. The pipeline performs Doppler correction, flat and dark fielding, flux calibration, and wavelength solution. First-order STIS data were deemed acceptable in post-pipeline calibrated form from the archive.

### *2.1.3. Goddard High Resolution Spectrograph*

All data were recalibrated using the most recent version of the GHRS pipeline and calibration files. Changes especially in the latter make this recalibration prefer-

able to using archived calibrated data. During the recalibration process, the GHRS wavelength scale was improved using calibration lamp and SPYBAL exposures taken immediately before or after the science exposure. The pipeline combines sub-stepped exposures, performs flat and dark fielding, and provides flux calibration and a wavelength solution. Much of the data used here were taken as part of surveys for low-redshift Ly $\alpha$  absorption (Penton et al. 2000a,b, 2004). The basic data reduction steps were repeated here, but following the same procedure described in these papers, to which the reader is referred for further discussion of the data characteristics.

TABLE 1  
DATASETS

Target	Instrument <sup>a</sup>	Diagnostic line	dataset(s)	aux dataset(s)	$t_{\text{exp}}$ (ksec)	obsv date	PI/PEP ID
ESO 141-G55	FUSE	OVI	i9040104		11.1	9/99	Savage
	GHR	CIV	z3i7010dt	z3i7010ct	4.6	10/96	Savage/6451
	GHR	CIV	z3i7010bt	z3i7010ct	6.5	10/96	Savage/6451
	GHR	NV	z3i70105t	z3i7010ct	9.8	10/96	Savage/6451
	GHR	NV	z3e70204t	z3e70203t	7.8	8/96	Stocke/6593
	GHR	NV	z3e70206t	z3e70205t	7.8	8/96	Stocke/6593
Fairall 9	FUSE	OVI	p1010601		4.0	7/00	Savage
	GHR	NV	z3e70406t	z3e70405t	6.9	8/96	Stocke/6593
	GHR	NV	z3e70404m	z3e70403t	14.4	8/96	Stocke/6593
	GHR	CIV	z26o020bt	z26o020at	8.1	4/94	Savage/5300
	GHR	NV	z26o0208n	z26o0207t,at	8.1	4/94	Savage/5300
H 1821+643	FUSE	OVI	p1016402		47.3	7/00	Savage
	E140M	CIV,NV	o5e704010-e0		24.5	3/00	Jenkins/8165
	E140M	CIV,NV	o5e703010-e0		24.5	7/99	Jenkins/8165
	G140M	CIV	o5fe01010		3.2	6/99	Stocke/8182
	GHR	CIV	z27n010bn	z27n010at,ct	16.1	4/94	Lu/5299
	GHR	NV	z27n0108m	z27n0107t,9t	10.4	4/94	Lu/5299
	GHR	NV	z15f0208m	z15f0207t	7.3	4/93	Savage/4094
Mrk 110	FUSE	OVI	p1071302		7.7	2/01	Moos
	G140M	NV	o4n302010		1.1	5/99	Côté/7295
	G140M	NV	o4n352010		1.1	10/99	Côté/7295
Mrk 116	FUSE	OVI	p1080901		38.2	2/01	Moos
	GHR	NV	z3ig020bt	z3ig020at	8.3	12/96	Lequeux/6710
	GHR	NV	z3ig0208m	z3ig0207t	6.5	12/96	Lequeux/6710
	GHR	NV	z3ig0205t	z3ig0204t	6.5	12/96	Lequeux/6710
	GHR	NV	z3ig010bt	z3ig010at	8.3	11/96	Lequeux/6710
	GHR	NV	z3ig0108m	z3ig0107t	6.5	11/96	Lequeux/6710
	GHR	NV	z3ig0105t	z3ig0104t	6.5	11/96	Lequeux/6710
	GHR	NV	z3ig0305t	z3ig0304t	3.5	11/96	Lequeux/6710
Mrk 279	FUSE	OVI	p1080303		17.8	12/99	Moos
	FUSE	OVI	p1080304		3.2	1/00	Moos
	GHR	NV	z3e70304t	z3e70303t,5t	6.1	1/97	Stocke/6593
	GHR	NV	z3e70306t	z3e70305t,7t	6.1	1/97	Stocke/6593
	GHR	NV	z3e70308t	z3e70307t,9t	6.1	1/97	Stocke/6593
	GHR	NV	z3e7030at	z3e70309t	1.5	1/97	Stocke/6593
Mrk 290	FUSE	OVI	p1072901		6.2	3/00	Moos
	GHR	NV	z3kh0104t	z3kh0103t	1.8	1/97	Wakker/6590
	GHR	NV	z3kh0105t	z3kh0103t,6t	2.8	1/97	Wakker/6590
	GHR	NV	z3kh0107t	z3kh0106t	2.5	1/97	Wakker/6590
Mrk 335	FUSE	OVI	p1010203		28.9	12/99	Savage
	FUSE	OVI	p1010204		46.2	11/00	Savage
	GHR	NV	z1a60304n	z1a60303t	14.8	9/93	Stocke/3584
Mrk 421	FUSE	OVI	p1012901		8.2	12/00	Savage
	GHR	NV	z2ia0104t	z2ia0103t	15.7	2/95	Stocke/5715
Mrk 478	FUSE	OVI	p1110909		9.5	1/29	Kriss
	G140M	NV	o4ec14040,50,60		7.6	3/99	Stocke/7345
Mrk 509	FUSE	OVI	x0170101,2		42.2	11/99	Sembach
	GHR	NV	z3e70704t	z3e70703t	4.7	10/96	Stocke/6593
	GHR	CIV	z26o0108t	z26o0107t,9t	8.1	8/94	Savage/5300
	GHR	NV	z1790208m	z1790207t,9m	6.9	4/93	Savage/3463

TABLE 1—*Continued*

Target	Instrument <sup>a</sup>	Diagnostic line	dataset(s)	aux dataset(s)	$t_{\text{exp}}$ (ksec)	obsv date	PI/PEP ID	
Mrk 771	FUSE	OVI	p1072301		6.1	1/01	Moos	
	G140M	NV	o4ec07030,40		5.8	7/99	Stocke/7345	
	G140M	NV	o4n305010		2.0	5/99	Côté/7295	
Mrk 817	FUSE	OVI	p1080401,2		11.5	2/00	Moos	
	FUSE	OVI	p1080404		16.4	2/01	Moos	
	GHRM	NV	z3e70104t	z3e70103t	9.5	1/97	Stocke/6593	
	GHRM	NV	z3e70106t	z3e70105t	8.8	1/97	Stocke/6593	
	GHRM	NV	z3e70108t	z3e70107t	8.5	1/97	Stocke/6593	
Mrk 876	FUSE	OVI	p1073101		20.9	10/99	Moos	
	G140M	NV	o4n308010		2.3	9/98	Cote/7295	
Mrk 926	FUSE	OVI	p1074001		4.0	6/00	Moos	
	G140M	NV	o4ec12020,10		3.9	7/99	Stocke/7345	
Mrk 1095	FUSE	OVI	p1011201,2		13.9	11/00	Savage	
	FUSE	OVI	p1011203		16.9	12/00	Savage	
	GHRM	NV	z3e7060at	z3e70609t	2.6	12/96	Stocke/6593	
	GHRM	NV	z3e70608m	z3e70607t	6.1	12/96	Stocke/6593	
	GHRM	NV	z3e70606t	z3e70605t	6.1	12/96	Stocke/6593	
	GHRM	NV	z3e70604t	z3e70603t	6.1	12/96	Stocke/6593	
NGC 3783	FUSE	OVI	p1013301		23.4	2/00	Savage	
	E140M	CIV,NV	o57b01010,20,30		7.6	2/00	Kraemer/8029	
	GHRM	CIV	z2nf0107t	z2nf0106t,9t	2.2	4/95	Maran/5724	
	GHRM	CIV	z2nf0108t	z2nf0106t,9t	2.2	4/95	Maran/5724	
	GHRM	CIV	z1av0107t	z1av0106t,9t	2.4	1/94	Maran/3936	
	GHRM	CIV	z1av0108t	z1av0106t,9t	2.4	1/94	Maran/3936	
	GHRM	CIV	z11q0107m	z11q0106m,8m	2.2	2/93	Maran/1160	
	GHRM	CIV	z11q0109m	z11q0108m,am	2.0	2/93	Maran/1160	
	GHRM	NV	z1790308m	z1790307t,9m	8.1	2/93	Savage/3463	
	NGC 4151	FUSE	OVI	p1110505		9.1	3/00	Kriss
E140M		CIV,NV	o61l01010,20		9.4	3/00	Kriss/8608	
E140M		CIV,NV	o57801030,40		5.5	7/99	Hutchings/8019	
GHRM		CIV	z2bs0405p-ap	z2bs0404p	9.2	3/96	Weymann/5169	
GHRM		CIV	z2bs0205t-8t,at,bt	z2bs0204t,9t	9.2	10/94	Weymann/5169	
GHRM		CIV	z1li0205t-8t,at,bt	z1li0204t,9t	9.2	1/94	Weymann/4880	
GHRM		CIV	z0yd0209t	z0yd0207t,8t,at	1.4	7/92	Weymann/1141	
GHRM		CIV	z0yd020bm	z0yd020at	1.4	7/92	Weymann/1141	
GHRM		CIV	z0yd020cm	z0yd020dm	1.4	7/92	Weymann/1141	
GHRM		CIV	z0yd020em	z0yd020dm	1.4	7/92	Weymann/1141	
GHRM		CIV	z0yd020fm	z0yd020gm	1.4	7/92	Weymann/1141	
GHRM		CIV	z0yd020hm	z0yd020gm	1.4	7/92	Weymann/1141	
NGC 5548		FUSE	OVI	p1014601		20.9	6/00	Savage
		E140M	CIV,NV	o4ll010d0,c0		4.7	3/98	Kraemer/7572
	GHRM	CIV	z2ws020at,9t	z2ws0208t	9.9	2/96	Savage/5889	
	GHRM	NV	z2ws0207t	z2ws0205t,6t	4.6	2/96	Savage/5889	
PG 0804+761	FUSE	OVI	p1011901		5.9	10/99	Savage	
	FUSE	OVI	p1011903		1.5	1/00	Savage	
	G140M	NV	o4ec06010		4.9	2/98	Stocke/7345	
	G140M	NV	o4n301010		2.4	2/98	Côté/7295	
PG 0953+414	FUSE	OVI	p1012201		26.7	5/00	Savage	
	FUSE	OVI	p1012202		15.9	12/99	Savage	
	E140M	CIV,NV	o4x001010,20,2010		244.8	12/98	Savage/7747	

TABLE 1—*Continued*

Target	Instrument <sup>a</sup>	Diagnostic line	dataset(s)	aux dataset(s)	$t_{\text{exp}}$ (ksec)	obsv date	PI/PEP ID
PG 1116+215	FUSE	OVI	p1013101		11.0	4/00	Savage
	FUSE	OVI	p1013103,4,5		43.6	4/01	Savage
	E140M	CIV,NV	o5a301010,20,2010,20		199.2	5/00	Sembach/8097
	G140M	NV	o4ec04010,20		2.6	5/00	Stocke/7345
PG 1211+143	FUSE	OVI	p1072001		52.2	4/00	Moos
	G140M	NV	o4ec08040,30		5.8	7/99	Stocke/7345
PG 1259+593	FUSE	OVI	p1080101		14.0	2/00	Moos
	FUSE	OVI	p1080102		0.5	12/00	Moos
	FUSE	OVI	p1080103		35.4	1/01	Moos
	FUSE	OVI	p1080104–9		303.5	3/01	Moos
	G140M	NV	o4n307020		1.8	3/99	Côté/7295
PG 1351+640	FUSE	OVI	p1072501		25.1	1/00	Moos
	G140M	NV	o4ec54010		8.5	8/00	Stocke/7345
PKS 2005-489	FUSE	OVI	p1073801		7.7	8/00	Moos
	G140M	NV	o4ec09040,30		6.1		Stocke/7345
PKS 2155-304	FUSE	OVI	p1080701		17.7	10/99	Moos
	FUSE	OVI	p1080705		34.8	10/99	Moos
	E140M	CIV,NV	o5by02010,20		14.3	9/00	Shull/8125
	E140M	CIV,NV	o5by01010,20		14.3	11/99	Shull/8125
	GHRM	CIV	z2ws0107p,8p	z2ws0106p	6.7	10/95	Savage/5889
	GHRM	NV	z1aw0106t,7t,8m	z1aw0105t	5.3	5/93	Bogess/3965
Q1230.8+0115	FUSE	OVI	p1019001		4.0	6/00	Savage
	E140M	CIV,NV	o56a01010,20,2010,20		27.2	1/99	Rauch/7737
	GHRM	NV	z3cj0105t	z3cj0104t	5.9	7/96	Rauch/6410
	GHRM	NV	z3cj0108t	z3cj0107t	5.9	7/96	Rauch/6410
3C273	FUSE	OVI	p1013501		29.8	4/00	Savage
	GHRM	CIV	z1d00109t	z1d00108t,at	1.1	12/93	Weymann/4883
	GHRM	CIV	z1d0010bt-dt	z1d0010at,et	3.3	12/93	Weymann/4883
	GHRM	NV	z1760105t	z1760103t,4t,6t	1.2	11/93	Weymann/3951
	GHRM	NV	z1760107t,8t	z1760106t	2.4	11/93	Weymann/3951
	GHRM	NV	z0gu010om	z0gu010nm,pm	2.9	2/91	Weymann/1140
	GHRM	CIV	z0gu010cm	z0gu010am,bm,dm	1.4	2/91	Weymann/1140
	3C351	FUSE	OVI	q1060101		17.0	10/99
FUSE		OVI	q1060102		3.1	2/00	le Brun
FUSE		OVI	p1080801		53.5	5/01	Moos
E140M		CIV,NV	o57902010-80		18.6	2/00	Jenkins/8015
E140M		CIV,NV	o57901010-80,3020-60		34.2	6/99	Jenkins/8015
Ton S180	FUSE	OVI	p1010502		12.3	12/99	Savage
	G140M	NV	o4ec02010,20		4.1	7/99	Stocke/7345
VII Zw 118	FUSE	OVI	p1011604		15.1	10/99	Savage
	FUSE	OVI	p1011605		9.8	11/99	Savage
	FUSE	OVI	p1011606		7.2	1/00	Savage
	G140M	NV	o4ec13010		9.5	11/97	Stocke/7345

<sup>a</sup>“E140M” and “G140M” refer to echelle and first-order modes of STIS, whereas “GHRM” refers in all cases to the G160M first-order mode of that instrument.

### 3. Observational Results

#### 3.1. Summary of Observations

The data are of widely varying quality, but show good agreement with previous measurements. The dataset as a whole is well-suited to the study of global trends. Unfortunately, the values of  $N(\text{N V})/N(\text{O VI})$  do not seem to favor any of the production mechanisms modeled in the literature. We find that there may be a weak trend for lower  $N(\text{N V})/N(\text{O VI})$  at more positive velocities, which can be thought of as a higher ionization state at more positive velocity (redshifted) gas. Previous authors have discussed such a signature as an offset in mean velocity between the Li-like ion absorption. Although this is an acceptable way to think of the situation, it implies that the absorption profiles are the same, which is not always true.

Table 2 summarizes the data for the 34 lines of sight. The total (integrated) column densities for the O VI, N V, and, where available, C IV absorption lines are listed along with the velocity range  $[v_-, v_+]$  over which the line was integrated. For N V and C IV, the column densities calculated from the two lines of the doublet agree to within errors, and there is no evidence that a saturation correction for instrumental smearing is required. Thus, the weighted mean column density is used in subsequent analysis. Also listed are the  $3\sigma$  upper limit equivalent widths for Cl I and H<sub>2</sub> lines, or in cases where H<sub>2</sub> absorption was removed from the O VI line, the equivalent width is listed. N V is typically weak, but many sightlines have reliable detections. Table 2 also lists the slope of a

line fitted to the log of the column density ratio  $N(\text{N V})/N(\text{O VI})$ , a procedure discussed in the next section. Selected characteristics of some sightlines are noted in Appendix A.

Figure 1 shows two example sightlines, towards 3C273 and ESO141-G55. The upper panel of each plot shows the normalized intensity of the three absorption lines (C IV was available for these particular sightlines), and the lower panel shows the log of the apparent column density ratio as a function of velocity. The column density ratio is only used for each sightline over the velocity range for which the errors are sufficiently small and there is appreciable absorbing column. (Ratios are generally restricted to points with less than 0.5 dex  $(\text{km s}^{-1})^{-1}$  error, which in practice limited errors to  $\lesssim 0.3$  dex  $(\text{km s}^{-1})^{-1}$  in most sightlines because the errors climb quickly in the line wings.) Some of the sightlines also include high velocity clouds, for which the column density ratio can occasionally be measured. As discussed below, these objects are interesting because they may consist of old material accreting onto the Galaxy for the first time, or possibly material ejected to particularly high altitudes by a Galactic fountain.

Although the main focus of this study is the ratios of column densities, brief discussion of the total line-of-sight absorption measurements and how they relate to previous measurements is merited. Figure 2 shows the distributions of total column densities of N V and O VI. The medians of the distributions are  $2.6 \times 10^{14} \text{ cm}^{-2}$  of O VI and  $2.8 \times 10^{13} \text{ cm}^{-2}$  of N V. Savage et al. (2003) find a mean O VI column density of  $2.3 \times 10^{14} \text{ cm}^{-2}$  in 91 sightlines including



TABLE 2  
SIGHTLINES

Target	l	b	EW CII (mÅ)	EW H <sub>2</sub> λ1031 (mÅ)	EW H <sub>2</sub> λ1032 (mÅ)	v <sub>±</sub> (km s <sup>-1</sup> )	log N OVI λ1032	δ log N	log N NV λ1239	δ log N	log N NV λ1242	δ log N	log N CIV λ1548	δ log N	log N CIV λ1551	δ log N	slope NV OVI	δslope NV OVI	
Parkes 2155-304	17.7	-52.3	< 5.6	< 9	< 6	-300	150	14.52	.07	13.53	.35	13.25	>1	14.21	.06	14.16	.13	-.0005	.0003
NGC 5548	32.0	70.5	< 36	39± 14	< 27	-150	100	14.52	.11	13.73	.17	13.50	.65	14.43	.05	14.45	.08	-.0034	.0003
Markarian 509	36.0	-29.9	< 11	81± 12 <sup>b</sup>	21± 32	-100	115	14.68	.05	13.86	.14	13.73	.33	14.39	.05	13.46	.07	+0.0005	.0001
Markarian 478	59.2	65.0	< 32	25± 22	< 26	-150	100	14.50	.12	13.47	.34	13.53	.60	-	-	-	-	-.0039	.0006
Markarian 1513	63.7	-29.1	< 43	73± 20	< 78	-100	100	14.33	.17	13.19	.66	13.69	.42	-	-	-	-	-.0035	.0020
Markarian 926	64.1	-58.8	<225	<257	<140	-65	100	14.26	.65	13.00	.97	<14.3	-	-	-	-	-	-	-
Markarian 290	91.5	48.0	< 77	<122	< 42	-200	200	14.48	.22	13.56	.42	13.28	1.	-	-	-	-	+0.0016	.0016
H 1821+643	94.0	27.4	< 25	35± 10	< 13	-150	100 <sup>c</sup>	14.54	.08	14.09	.10	14.20	.15	14.39	.04	14.40	.07	+0.0002	.0003
Markarian 876	98.3	40.4	< 12	85± 10	24± 22	-200	150 <sup>c</sup>	14.60	.08	13.58	.35	13.75	.46	-	-	-	-	-.0024	.0002
Markarian 817	100.3	53.5	< 9.5	< 11	< 10	-200	150 <sup>c</sup>	14.56	.04	13.87	.10	12.93	>1	-	-	-	-	-.0007	.0001
Markarian 335	108.8	-41.4	< 7.0	73± 6	22± 14	-100	100	14.06	.16	<13.5	-	13.10	.50	-	-	-	-	-	-
PG 1351+640	111.9	52.0	< 27	62± 20	< 29	-175	175	14.57	.12	<14.2	-	12.80	>1	-	-	-	-	-	-
Markarian 279	115.0	46.9	< 11	< 13	< 18	-200	100	14.52	.08	13.74	.15	13.56 <sup>d</sup>	.40	-	-	-	-	-.0025	.0001
PG 1259+593	120.6	58.1	< 14	10± 16	< 5	-175	200 <sup>c</sup>	14.35	.06	13.25	1.	14.22 <sup>d</sup>	.30	-	-	-	-	-.0038	.0051
Markarian 1502	123.8	-50.2	< 70	60± 60	51± 40	-50	85	14.00	.27	13.25	.60	<13.8	-	-	-	-	-	-.0021	.0075
PG 0804+761	138.3	31.0	< 16	104± 14	22± 26	-125	100	14.48	.09	13.34	.27	<13.9	-	-	-	-	-	-.0109	.0004
Ton S180	139.0	-85.1	< 25	< 23	< 16	-95	100	14.39	.10	13.10	.61	12.90	>1	-	-	-	-	-.0053	.0008
Zwicky VII 118	151.4	26.0	< 19	73± 8	32± 20	-100	75	14.21	.13	12.30	>1	13.40	.86	-	-	-	-	-	-
NGC 4151	155.1	75.1	< 29	108± 20 <sup>b</sup>	< 15	-100	100 <sup>c</sup>	14.12	.09	12.96	1.	- <sup>d</sup>	-	14.01	.06	13.75	.34	-.0021	.0027
Markarian 116	160.5	44.8	< 21	55± 14	< 78	-150	100	14.40	.22	13.00	>1	13.60	.58	-	-	-	-	-	-
Markarian 110	165.0	44.4	<288	50±100	<140	-100	100	14.30	.32	13.28	.83	<14.4	-	-	-	-	-	+0.0092	.0086
PG 0953+414	179.8	51.7	< 13	< 9	< 9	-125	250 <sup>c</sup>	14.50	.08	13.26	.87	13.77	.53	13.97	.13	13.64	.50	+0.0068	.0036
Markarian 421	179.8	65.0	< 18	31± 46	< 16	-150	200 <sup>c</sup>	14.44	.12	13.30	.48	12.30 <sup>d</sup>	1.	-	-	-	-	-.0067	.0036
NGC 985	180.8	-59.5	< 36	34± 10	< 15	-100	100	14.32	.12	13.41	.32	13.79	.25	-	-	-	-	-.0022	.0002
Markarian 1095	201.7	-21.1	< 12	115± 10	< 20	-50	50	13.81	.25	13.32	.28	13.68	.23	-	-	-	-	-.0156	.0007
PG 1116+215	223.4	68.2	< 8	15± 20	< 9	-50	350	14.59	.10	13.89	.27	13.73	.74	14.31	.10	14.35	.14	-.0000	.0003
PG 1211+143	267.6	74.3	< 11	49± 6	< 11	-100	100	14.08	.17	13.64	.18	14.01 <sup>d</sup>	.15	-	-	-	-	-.0035	.0004
PG 1229+204	269.4	81.7	<137	< 58	< 54	-50	150	14.57	.13	13.44	.31	13.72	.30	-	-	-	-	-.0020	.0014
NGC 3783	287.5	23.0	< 17	149± 19 <sup>b</sup>	95±165	-100	100	14.52	.09	13.23	.72	12.70	>1	14.30	.06	14.26	.10	-.0041	.0006
3C273	290.0	64.4	< 4.5	27± 6	< 8	-110	275	14.78	.04	13.94	.11	13.88	.25	14.47	.03	14.50	.05	-.0004	.0001
Fairall 9	295.1	-57.8	<230	< 90	< 83	-100	250	14.51	.20	13.40	.36	13.78 <sup>d</sup>	.27	14.19	.10	14.43	.10	-.0011	.0047
ESO 141-G55	338.2	-26.7	< 11	43± 12	27± 16	-100	100	14.49	.08	13.68	.15	13.77	.23	14.41	.04	14.55	.05	-.0020	.0001
Markarian 1383	349.2	55.1	< 19	15± 30	< 16	-100	160	14.48	.08	13.85	.12	13.80	.25	-	-	-	-	-.0009	.0001
Parkes 2005-489	350.4	-32.6	< 18	< 25	< 23	-100	250	14.88	.05	14.05	.07	13.94	.17	-	-	-	-	+0.0031	.0002

<sup>a</sup>Upper limit equivalent widths are 3σ, and errors are 2σ.

<sup>b</sup>Complex structure in H<sub>2</sub>: multiple components removed.

<sup>c</sup>In a few sightlines, the range over which the line ratio logN(NV)/logN(OVI) had to be restricted because of low signal-to-noise in the NVline. The particular sightlines and their restricted ranges are: H 1821+643, [-120,0]; Markarian 421, [-60,50]; Markarian 817, [-200,50]; Markarian 876, [-40,100]; NGC 4151, [-25,60]; PG 0953+414, [-50,10]; PG 1259+593, [-30,50].

<sup>d</sup>line contaminated.

these, but omit the high velocity gas. Theoretical models of evaporating gas predict  $\sim 2 \times 10^{13} \text{ cm}^{-2}$  of O VI and  $\sim 2 \times 10^{12} \text{ cm}^{-2}$  of N V per interface or cloud, models of cooling gas predict a few  $\times 10^{14} \text{ cm}^{-2}$  of O VI and a few  $\times 10^{13} \text{ cm}^{-2}$  of N V, and finally turbulent mixing layer models predict  $10^{11}$ - $10^{12} \text{ cm}^{-2}$  of O VI and  $10^{10}$ - $10^{11} \text{ cm}^{-2}$  of N V. (See Paper I for a complete description of the different models.) The current observations cannot distinguish between the models based on column density alone, although the large number of turbulent mixing layers required is somewhat worrisome. As described in Paper I and in the following section, the trends of the column density ratios with velocity can be a more powerful diagnostic of the physical production mechanism for Li-like ions.

Figure 3 compares the measured equivalent widths of some of the sightlines in this work to previously measured values. Each point represents a single sightline, and measurements of C IV, N V, and O VI are included in the plot. There is a slight trend towards systematically higher values in this study than previous work. This results because previous studies arbitrarily cut off absorption at some velocity in an attempt to isolate Galactic halo gas from high velocity clouds (HVCs). Our study excluded high velocity gas only when that gas was clearly separated in velocity. The effect of arbitrary velocity cutoffs is seen in two separate reportings of O VI towards ESO141-G55 by other authors (Savage et al. 2000a; Sembach et al. 1999). The higher equivalent width value resulted from a less restrictive velocity cutoff, and that higher value more nearly agrees with the value found in this work.

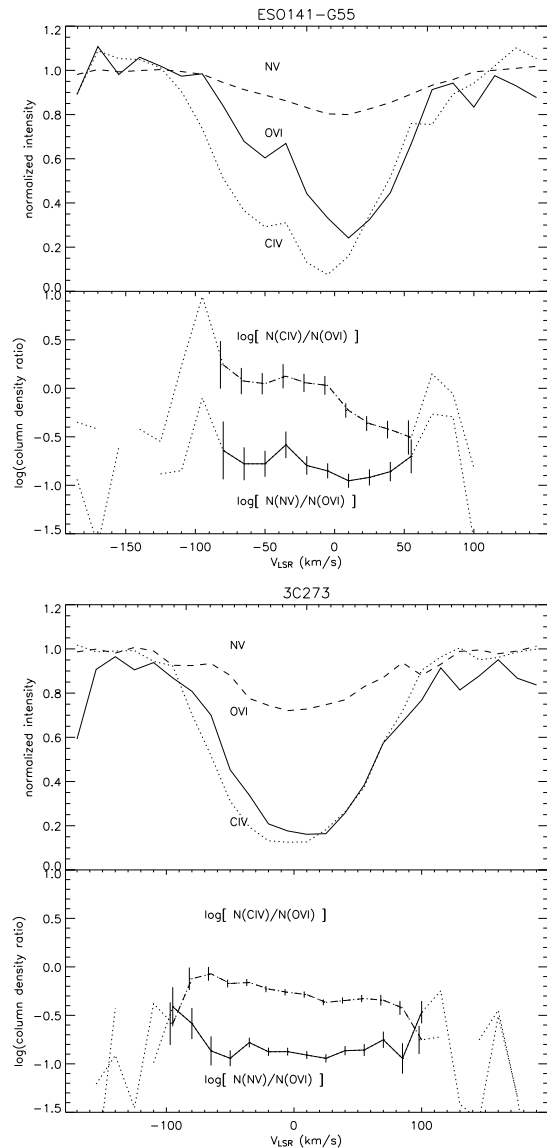


Fig. 1.— Example sightlines. The upper panel of each plot shows the normalized intensity of the three absorption lines, and the lower panel shows the log of the apparent column density ratio as a function of velocity ( $15 \text{ km s}^{-1}$  bins). The column density ratio is only used for each sightline over the velocity range for which the errors are sufficiently small, and where there is appreciable absorbing column (solid line). Dashed lines indicate regions where the signal-to-noise (column density) is too low to use the line ratio.

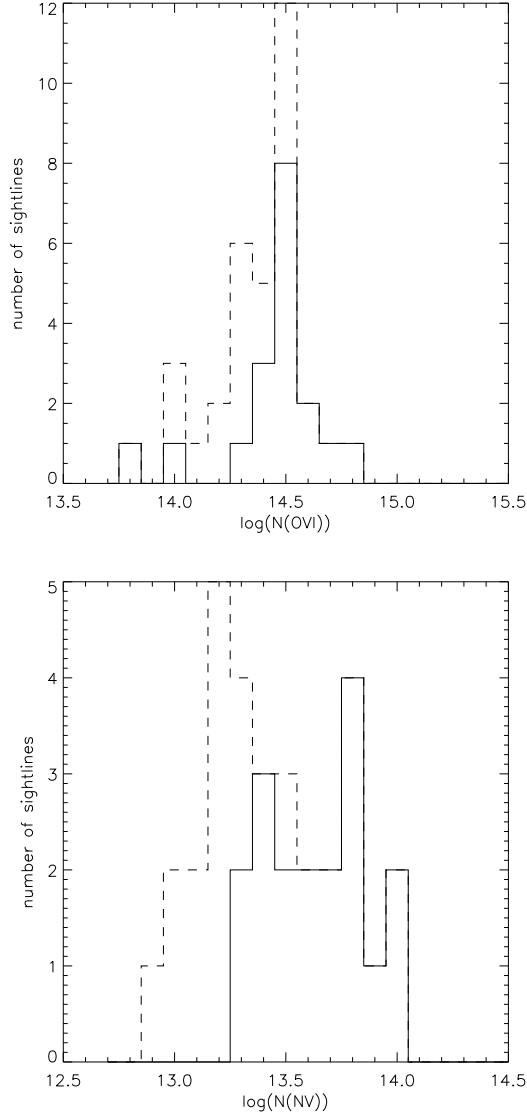


Fig. 2.— Distributions of total column density of N V and O VI along the 34 sightlines for which measurements could be made (dotted line). The distribution of column density for the sightlines with best measured  $N(\text{N V})$  ( $\delta N(\text{N V}) < 0.35$  dex) is shown as a solid line, and is naturally weighted towards the higher column densities. See text for properties.

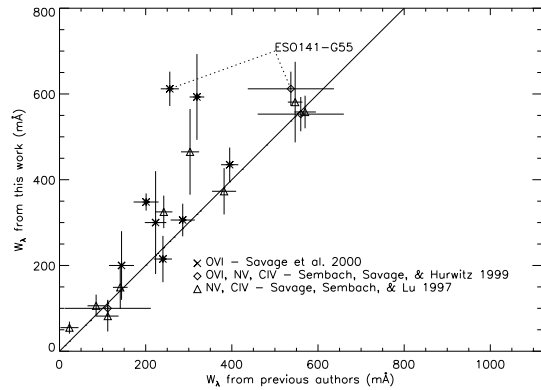


Fig. 3.— Comparison of equivalent widths for C IV, N V, and O VI measured in this and previous studies (Savage et al. 2000a; Sembach et al. 1999; Savage et al. 1997). Each point represents a single sightline. The solid line shows a 1:1 correspondence. The effect of arbitrary velocity cut-offs is shown for ESO141-G55 (two different cut-offs from two different articles). Our analysis often gives higher equivalent widths because of these cutoffs. All O VI column densities also agree within errors with Savage et al. (2003) and Wakker et al. (2003), taking into account velocity integration ranges.

### 3.2. Column Density Ratios

All of the sightlines for which all three ions are measurable are combined in Figure 4 and compared to predictions from several generic models. The distribution of velocity-resolved  $\log[N(\text{N V})/N(\text{O VI})]$  is shown in Figure 5. In Paper I, it was shown how the ratios of the column densities of Li-like ions could be used to distinguish between various theoretical models of the production of these ions. For example, models of thermally conducting, evaporating gas can be distinguished from turbulent mixing layers. Unfortunately, the data span most of the range allowed by the models, and the predominance of one type of model in the Galactic halo cannot be determined. The large thermal width of gas at several  $10^5$  K, compared to the velocity separation of the different physical processes which almost certainly exist along these lines of sight, precludes using Li-like ion ratios to distinguish between models in the two-dimensional space shown in Figures 4 and Paper I. It is important to note that, in Figure 5 and in subsequent analysis, the statistical properties of the N V/O VI distribution do not change with the inclusion or exclusion of lower signal-to-noise sightlines.

Table 3 lists the average column densities and column density ratios for this sample of halo sightlines, as well as the RMS dispersion of those quantities. The total, or integrated, column density along each line of sight is calculated, and the log of that quantity is averaged over all sightlines. The ratio of integrated column density is taken for each sightline, and the log of that ratio is also averaged over all sightlines. Finally, the column density ratio is

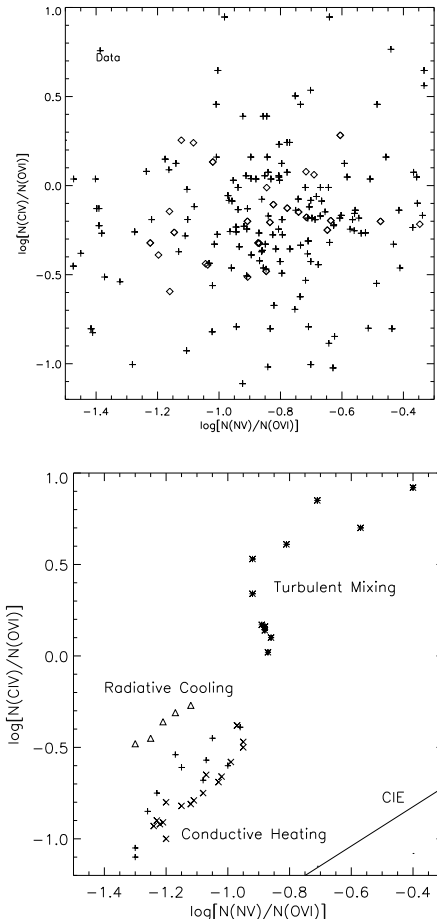


Fig. 4.— First panel: Column density ratios for the sightlines along which all three ions were measured. Each cross is a  $15 \text{ km s}^{-1}$  velocity resolution element. The dark diamonds are the velocity-integrated line ratios for each sightline. Darker symbols are data for the sightlines with highest signal-to-noise N V (error in total  $N(\text{N V}) < 0.35$  dex). Ratios should be compared with theoretical models presented in Paper I, repeated here as the second panel. The models are radiative cooling of galactic fountain gas (triangles, Shapiro & Benjamin 1993; Benjamin & Shapiro 1993), turbulent mixing layers (stars, Slavin et al. 1993), and conductive heating and evaporation of spherical clouds Böhringer & Hartquist (1987) and planar, clouds Borkowski et al. (1990) (“x”s), and in cooling supernova remnant shells (pluses, Slavin & Cox 1993; Shelton 1998). Also shown are the ion ratios for hot gas in collisional ionization equilibrium (Sutherland & Dopita 1993, CIE, solid line).

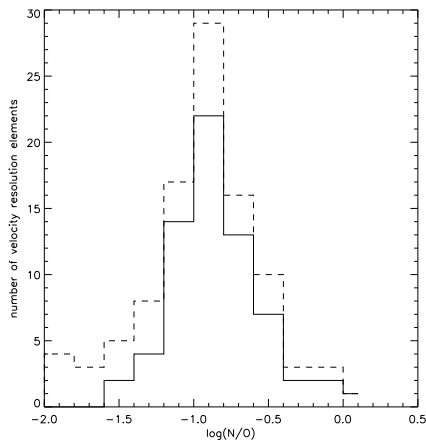


Fig. 5.— Distribution of velocity-resolved column density ratio  $\log[N(\text{N V})/N(\text{O VI})]$ . Each velocity resolution element is an instance of gas with a certain ion ratio, and this is a histogram of those instances. The range of observed ion ratio covers the entire range in theoretical models (Paper I). Variation in the ion ratio with velocity is discussed in the text. All sightlines are included in the dotted histogram, and only the highest signal-to-noise sightlines (error in total  $N(\text{N V}) < 0.35$  dex) are included in the solid histogram. Note that the statistical properties of the  $\text{N V}/\text{O VI}$  distribution do not change with the inclusion of lower signal-to-noise sightlines.

calculated for each velocity resolution element along the line of sight, and the log of that quantity is averaged, over all of the velocity bins along all lines of sight.

Although the integrated column density ratio of a given theoretical model is not as discerning a diagnostic as one might have hoped, different physical scenarios should have different ionization states as a function of velocity. Offsets in velocity between the Li-like ions, or gradients in the column density as a function of velocity, could provide a more powerful diagnostic of the physical state of the gas than the absolute value of the ion ratio, and this is modeled in § 4 and Paper I. The velocity of the absorbing gas can also be mapped onto Galactic altitude or radius, assuming that the halo gas corotates smoothly on cylinders with the disk.

Differences in velocity centroid and line width of the Li-like ions have been marginally detected in previous work. Sembach & Savage (1992) find an increase in line width with increasing ionization stage, and their data ( $\langle v \rangle$  in their Table 6) reveal a small trend for  $\text{N V}$  to be found at more negative velocities than  $\text{C IV}$ . Their data are more confused than the sample studied here because of the choice of sightlines. They use some stars towards the Galactic center which may not have the same gas kinematics as the outer disk (see Tripp et al. 1993), and some stars in the Magellanic Clouds, which may have their own hot gas kinematics (if those galaxies have fountain flows or outflows, the gas kinematics are in fact most likely to be opposite to those in our galaxy). In summary, there is evidence of differences in distribution between  $\text{C IV}$  and  $\text{N V}$ , but

TABLE 3  
AVERAGE HALO VALUES

ion or ratio	mean	RMS
$\log[N(\text{O VI})]$ <sup>a</sup>	14.54	0.19
$\log[N(\text{N V})]$	13.71	0.31
$\log[N(\text{C IV})]$	14.33	0.17
$\log[N(\text{N V})/N(\text{O VI})]$ <sup>b</sup>	-0.83	0.28
$\log[N(\text{C IV})/N(\text{O VI})]$	-0.28	0.18
$\log[N(\text{N V})/N(\text{O VI}) (\text{km s}^{-1})^{-1}]$ <sup>c</sup>	-0.76	0.64
$\log[N(\text{C IV})/N(\text{O VI}) (\text{km s}^{-1})^{-1}]$	-0.36	0.64

<sup>a</sup>Integrated column density along a sightline.

<sup>b</sup>Ratio of integrated column density along a sightline.

<sup>c</sup>Ratio of column density in each velocity resolution element along a sightline – see text.

the interpretation is not clear. The inner Galaxy sightlines of Tripp et al. (1993) are not inconsistent with Sembach & Savage (1992), but the trends are even less conclusive. Savage et al. (1997) also note that N V absorption is wider in velocity extent than C IV. Their data (their Table 4) show no particular velocity offset between C IV and N V.

In this dataset, there is some indication of a trend in the data towards higher mean ionization state (lower N V/O VI and lower C IV/O VI) in more redshifted gas. Many individual sightlines appear to have a trend of decreasing  $\log[N(\text{N V})/N(\text{O VI})]$  with velocity (see Figure 1, lower panels). This suggests the following analysis: the dataset is collapsed by making a linear fit to the ion ratio (in log space) as a function of velocity along each sight-

line. Clearly, there is no reason for the log of the ion ratio to have a linear dependence on velocity, but this allows a simple characterization of any general slope or trend with velocity along a sightline. Figure 6 is a histogram of the slopes fitted to the  $\log[N(\text{N V})/N(\text{O VI})]$  ratio along each sightline, and the individual fits are listed in Table 1. There appears to be an excess of sightlines with negative slopes, i.e. lower N(N V)/N(O VI) at more positive velocities. The mean slope is  $-0.0032 \pm 0.0022(\text{r}) \pm 0.0014(\text{sys}) \text{ dex } (\text{km s}^{-1})^{-1}$ . Random error (r) results from wavelength calibration, continuum fitting, signal-to-noise of the data, and the goodness of fitting a linear slope (which depends on the complexity of the given line of sight and the specific physical structures observed in absorption). Systematic error (sys) is a

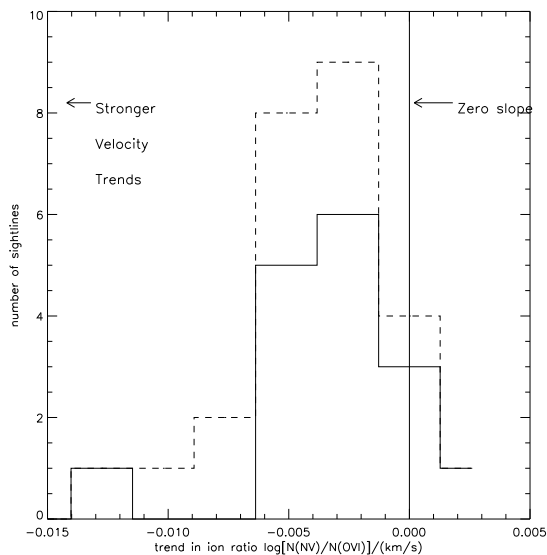


Fig. 6.— Distribution of slopes fitted to the ion ratio  $\log[N(\text{N V})/N(\text{O VI})]$  per unit velocity along each sightline. The mean slope is  $-0.0032 \pm 0.0022(\text{r}) \pm 0.0014(\text{sys}) \text{ dex } (\text{km s}^{-1})^{-1}$ . See text for discussion of random and systematic errors. All sightlines are included in the dotted histogram, and only the highest signal-to-noise sightlines (error in total  $N(\text{N V}) < 0.35 \text{ dex}$ ) are included in the solid histogram. The offset exists in the high signal-to noise data at the same significance as in the full dataset.

generous estimate of the remaining FUSE wavelength calibration problems and their impact on the relative wavelength calibration between FUSE and HST. Some of the lowest signal-to-noise sightlines have been omitted from this analysis, as indicated in the Appendix.

Figure 7 shows the fitted slopes to the column density ratio for each sightline as a function of Galactic longitude  $l$  and latitude  $b$ . There are no particular trends, which could result from selection effects or irregular sky coverage. There is a dipole moment in high-velocity cloud H I velocities in the northern 1<sup>st</sup> and 2<sup>nd</sup> quadrants, and more at positive velocities in the southern 3<sup>rd</sup> and 4<sup>th</sup> quadrants. However, trends in the column density *ratio* with velocity should not be directly affected by this dipole sky (see § 4.1 for more subtle effects), and no trends are seen here. Also singled out are sightlines that pass through HVC Complex C. Unlike the other major high-velocity clouds (the Magellanic Stream in particular) detected in this data and excluded from the general analysis, gas from Complex C cannot easily be discriminated by velocity from gas over the outer Galactic disk. Complex C gas is therefore included in our general analysis. Its low metallicity (0.1–0.3 solar, Wakker et al. 1999; Gibson et al. 2001; Collins et al. 2003) argues that Complex C is a mixture of Galactic fountain gas and more primordial infalling gas. Thus, one might expect different characteristics of the Complex C sightlines, but none are apparent. Either the trends along those sightlines are not being dominated by Complex C, or the trends do not form an appropriate diag-

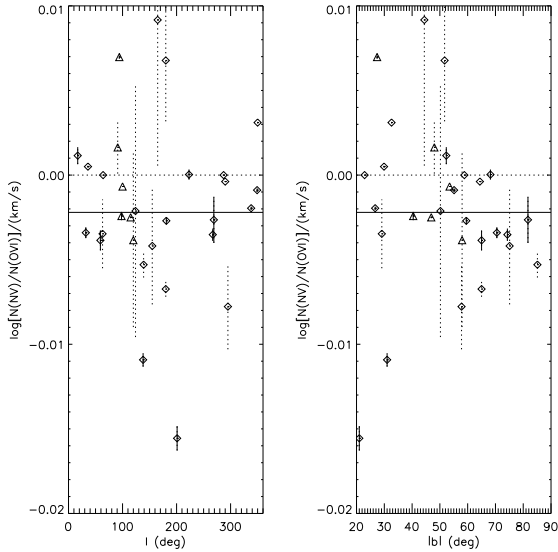


Fig. 7.— Fitted slopes to the column density ratio  $\log[N(\text{N V})/N(\text{O VI})]$  as a function of Galactic longitude  $l$  and latitude  $|b|$ . Sightlines that pass through high velocity cloud Complex C are distinguished by triangles. No systematic trends with Galactic location or with membership in Complex C are seen. (None are particularly expected, see Paper I.) The mean slope is marked with a solid line, and is negative, with lower  $N(\text{N V})/N(\text{O VI})$  at more positive velocities. Only the best data (error in total  $N(\text{N V}) < 0.35$  dex) are included in that average, but including all the sightlines doesn't change the mean within error.

nostic to distinguish different conditions in Complex C. The Li-like ionization structure in Complex C is apparently not significantly different from the rest of the Galactic halo.

### 3.3. Systematic and Instrumental Effects

Continuum placement is often the dominant error in absorption-line measurements, and it is especially important in the case of broad weak lines such as those expected from interstellar C IV, N V, and O VI. The continuum in these data was fitted in a region  $\sim 20 \text{ \AA}$  wide around the line of interest (the actual width was set by the wavelength coverage of the observation and the desire to omit strong emission features in the background source). The continuum was fitted as a fourth-order polynomial simultaneously with Gaussians for all absorption lines in the region. As demonstrated in Figure 8, the inclusion or exclusion of neighboring absorption features to the line of interest, especially weak features, was explored and the variation which this caused in the equivalent width of the line of interest was included in the experimental error. We also tried different order polynomials in the continuum fit and varied the size of the fitting region. Note that the Gaussian line-fitted equivalent widths were only used to assess error due to continuum fitting, and the final total column densities quoted below are integrated across velocity.

Various other interstellar absorption lines can contaminate the lines of interest, especially O VI. The N V and C IV doublets should be clear of other Galactic absorption, and for N V the doublets



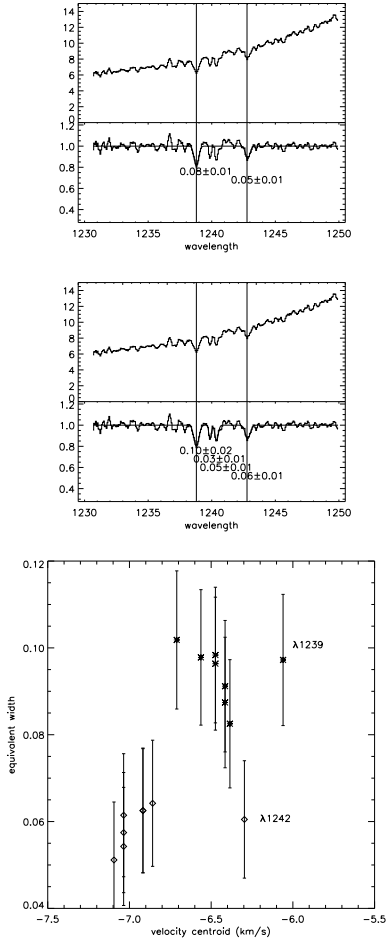


Fig. 8.— Continuum fitting procedure. The upper panels show the N V doublet ( $\lambda\lambda 1238, 1242$ ) towards ESO141-G55, and two weak Mg II lines between the N V lines. The equivalent widths ( $\text{\AA}$ ) of the N V lines are shown for the simultaneous fit of a 4<sup>th</sup>-order polynomial to the continuum and two or four Gaussian absorption features. The lower panel shows the fitted equivalent width and central velocity for each member of the N V doublet, for various combinations of continuum polynomial order and number of adjacent absorption features. The variation in the equivalent width is smaller than the plotted error calculated from the fit. The formal errors for the central velocity are several times the horizontal size of this plot and are not shown. The variation in the equivalent width was studied for each ion along each sightline. The continuum fit which yielded values closest to the mean was used in subsequent analysis, and the variation in equivalent width was incorporated into the quoted error in total column density.

were carefully examined for the presence of intergalactic Ly $\alpha$  or Ly $\beta$  absorption (as regards Ly $\beta$ , see in particular discussion of RXJ 1230.8+0115 in the Appendix). Absorption from H<sub>2</sub> and C II frequently contaminates the O VI 1038  $\text{\AA}$  line, so analysis was limited here to the 1032  $\text{\AA}$  line. Molecular hydrogen lines can also contaminate the 1032  $\text{\AA}$  line, specifically Lyman (6-0)P(3) 1031.19  $\text{\AA}$  and Lyman (6-0)R(4) 1032.35  $\text{\AA}$ . The strengths of these lines were measured using isolated H<sub>2</sub> lines of the same  $J$  level elsewhere in the FUSE spectrum, typically  $\sim 10$  lines for each rotational level for each sightline. The column density in that rotational level was calculated. The H<sub>2</sub> absorption is removed from the O VI absorption where relevant, and the error bars of those points increased accordingly. The strength of the H<sub>2</sub> lines or their upper limits are reported in Table 2. This process is more precise for the P(3) line, as it is not a particularly strong  $J=3$  line compared to other measurable lines in the bandpass. The R(4) line is one of the stronger  $J=4$  lines available in the FUSE long-wavelength segments, so the error in the column measured from weaker lines is larger. The R(4) line is much weaker than the P(3) line, however, and usually does not confuse the analysis. It should be noted that, in a few sightlines, more than one H<sub>2</sub> component was justified by inspection of other isolated lines in the FUSE bandpass. Incorrect subtraction of H<sub>2</sub> in this study is most likely to err towards underestimating the O VI column, because conservative determinations were made in situations where the H<sub>2</sub> absorption is complex. The presence of under-subtracted H<sub>2</sub> in the stronger line, at a velocity of  $-212 \text{ km s}^{-1}$  relative to O VI,

would decrease any trend of decreasing  $N(\text{N V})/N(\text{O VI})$ , so if there is such a systematic error, the correction of that error would only strengthen the trend.

The  $\text{Cl I } \lambda 1031.507$  absorption could also contaminate the  $\text{O VI}$  line. The  $\text{Cl I}$  column density was measured along each line of sight using other isolated lines in the FUSE bandpass. Only upper limits were obtained for this contamination, and no subtraction was performed. Unresolved saturated absorption components can be washed out in an absorption line, leading to an underestimate of the absorbing column density. This problem has been discussed in detail by various authors including Savage & Sembach (1991) and Jenkins (1996). The absorption lines of  $\text{C IV}$  and  $\text{O VI}$  can suffer from this effect, especially if these species are present in overionized gas. (In such cases, the gas is cooler than the temperatures at which these species dominate in collisional ionization equilibrium, so that the thermal widths are smaller or comparable to the FUSE resolution of  $\sim 15 \text{ km s}^{-1}$ ). Absorption features of  $\text{N V}$  are less susceptible, owing to the intrinsic weakness of the  $\text{N V } \lambda \lambda 1240$  doublet. As described in Savage & Sembach (1991), unresolved saturated absorption can be detected and corrected for by comparing two absorption lines of different oscillator strengths. In the case of the three doublets in this study, the apparent velocity-resolved column density can be compared in the two lines of the doublet, whose strengths differ by a factor of two.

Figure 9 shows the velocity-resolved apparent column density  $N_a(v)$  for the sightline that shows most clear evidence

of unresolved saturated absorption, ESO 141-G55. The weaker line of the doublet yields higher apparent column densities  $N_a(v)$  than the stronger line, by  $\lesssim 0.1$  dex ( $0.06 \pm 0.15$  dex for  $\text{N V}$  and  $0.1 \pm 0.1$  dex for  $\text{C IV}$ ). By the method of Savage & Sembach (1991), the  $\text{C IV}$  and  $\text{N V}$  total column densities should be corrected by approximately 0.1 dex. However,  $\text{O VI}$  probably also suffers from unresolved saturated components resulting in a similar correction. In almost all sightlines, the  $\text{O VI } 1038$  line is confused by  $\text{H}_2$  and  $\text{C II}$  absorption, so the correction cannot be reliably made. No corrections for unresolved saturation are applied to the data in this study, because the variation of column density ratio with velocity is of primary interest, and because the correction for  $\text{O VI}$  cannot be made in most cases with only a single absorption line. We explore the effects of unresolved saturated components below, and find it to be small.

Figure 10 shows the effect of unresolved absorption, in an analysis similar to Savage & Sembach (1991); the optical depth for  $\text{O VI}$  at the (probably unrealistically) lower limit temperature of 25,000 K is moderately underestimated by being underresolved by FUSE. At 10 times lower concentration,  $\text{N V}$  is accurately measured. In this worst-case scenario, the velocity-resolved column density can be off by quite a bit (more than the total apparent column density, because of the effects of instrumental smearing), but the effect is symmetric across the line. This effect cannot account for the large scatter in observed  $\text{N V}/\text{O VI}$  ratios (Figure 4). Most sightlines have lower quality data, and more realistic temperatures for the absorbing gas

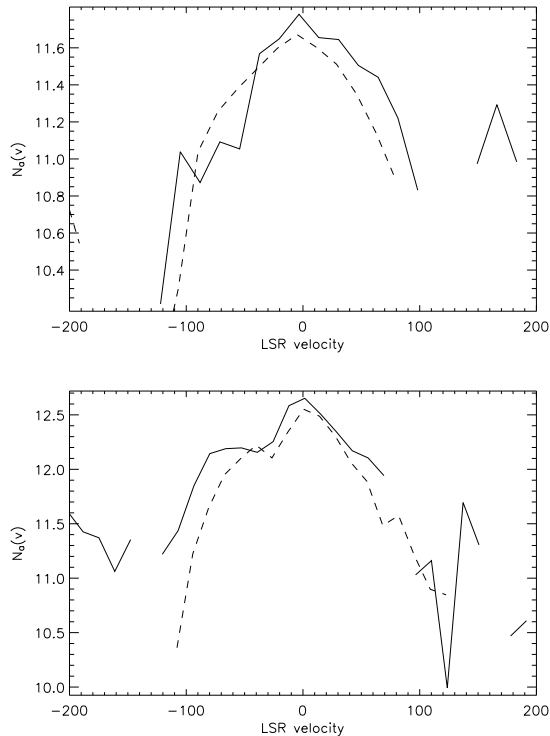


Fig. 9.— Apparent column density as a function of velocity for N V and C IV towards ESO141-G55. Column density calculated from the weaker line of each doublet (solid lines) is slightly greater than that calculated from the stronger line of the doublet (dashed lines), indicating unresolved saturated absorption components. For the instrumental resolution and degree of saturation in this case, the methods of Savage & Sembach (1991) indicate that the correction to be added to the larger column density is about the same as the difference in apparent column density between the two lines, or  $\lesssim 0.1$  dex ( $0.06 \pm 0.15$  dex for N V and  $0.1 \pm 0.1$  dex for C IV).

result in column density ratio corrections that, if they could be calculated for O VI, would be within the error bars. Wakker et al. (2003) estimate that, for a set of sightlines that includes this one, fewer than 20% of the sightlines should require saturation correction in O VI, and the correction would be less than 0.1 dex in those cases.

In the context of velocity-resolved data, it is more interesting to investigate the effect of saturation and instrumental smearing on the observed line ratio. The fourth panel of Figure 10 shows that for symmetric line profiles, this effect will decrease any trend of ion ratio as a function of velocity or wavelength. If the line profile is not symmetric, then saturation and instrumental smearing can affect the stronger O VI line more than the N V line, resulting in a small gradient in the observed ion ratio which is not present in the true ratio. Figure 11 illustrates this effect; we model a line with a sawtooth shape in  $N(v)$ , with typical O VI and N V column densities per  $\text{km s}^{-1}$  (see Table 3). Smearing has a small effect on the measured column, as seen in the top two panels, but the effect is similar between N V and O VI lines. The observed line ratio in the lower left panel shows a gradient not present in the true column density distribution, but that gradient is only  $\sim -0.0001$  dex  $(\text{km s}^{-1})^{-1}$ , smaller than the gradient measured in many of the sightlines in this study. Visual inspection of the data shows that  $\sim 1/3$  of the sightlines have an asymmetric O VI line profile with more column at more positive velocities, which in combination with instrumental smearing, could produce a small negative slope in the observed N V/O VI ratio. As for symmetric lines, the lower

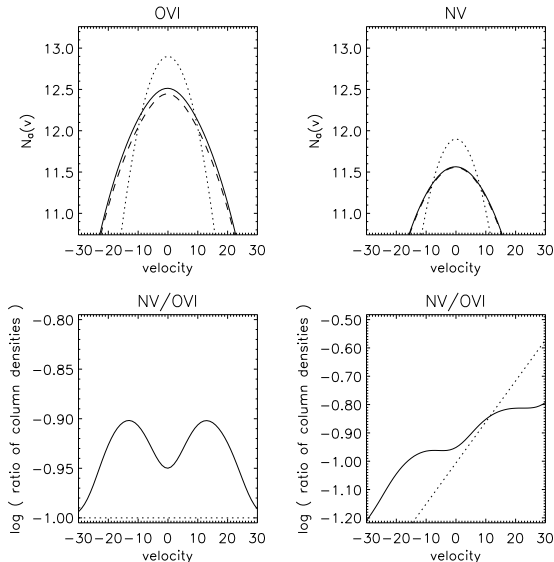


Fig. 10.— Modeled effect of unresolved lines shows that, in an unrealistically worst case, the velocity-resolved column density ratio can be miscalculated by 0.1 in the log. In this model, similar to the analysis of Savage & Sembach (1991), O VI at the unrealistically low temperature of 25,000 K is observed by FUSE. The apparent column density as a function of velocity  $N_a(v)$  is plotted in the upper left panel, as calculated from the stronger (dashed) and weaker (solid) line of the doublet. The true velocity-resolved column density  $N(v)$  is also plotted with a dotted line. The 0.1 dex difference in observed column density using the two members of the doublet is the largest saturation observed in C IV data in this study, so this is also a worst case. The upper right panel shows N V at the same temperature but 10 times lower concentration. The column density profile is blurred by the instrumental resolution but the total column would be accurately determined. The lower left panel shows the log of the ratio of observed column densities, which differs from the true ratio of -1 by 0.1 dex. More realistic temperatures and densities for the absorbing gas yield corrections  $\lesssim 10\%$ , which is well within the errors calculated from other sources. The lower right panel shows the true and observed log column density ratio for a situation in which the nitrogen central velocity is slightly offset from the oxygen. The effect of instrumental resolution is to decrease the observed trend of ion ratio as a function of velocity.

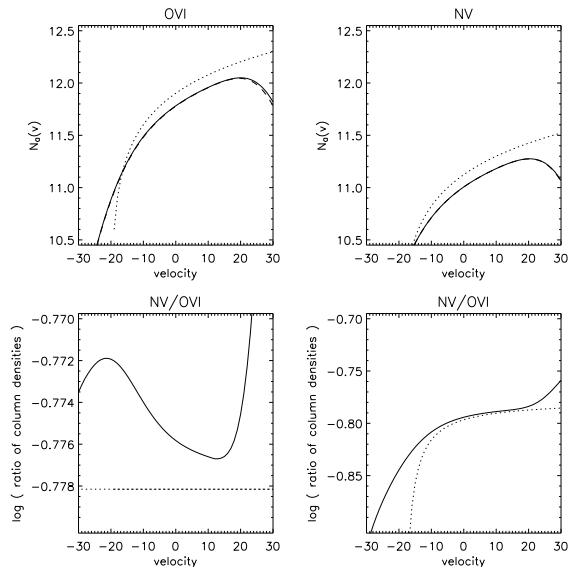


Fig. 11.— Modeled effect of saturation and instrumental smearing for an intrinsically asymmetric line. Panels are as Figure 10, for an absorption line with a sawtooth shape in  $N(v)$ , with typical O VI and N V column densities per  $\text{km s}^{-1}$  (see Table 3). Smearing has a small effect on the measured column, as seen in the top two panels, but the effect is similar between N V and O VI lines. The apparent column density as a function of velocity  $N_a(v)$  is plotted as calculated from the stronger (dashed) and weaker (solid) line of the doublet. The true velocity-resolved column density  $N(v)$  is also plotted with a dotted line. The observed line ratio in the lower left panel shows a gradient not present in the true column density distribution, but that gradient is only  $\sim 0.0001 \text{ dex (km s}^{-1}\text{)}^{-1}$ , smaller than the gradient measured in many of the sightlines in this study. As for symmetric lines, the lower right panel shows that asymmetric lines offset in velocity also cause gradients in the line ratio, and that instrumental smearing can decrease that gradient.

right panel shows that asymmetric lines offset in velocity also cause gradients in the line ratio, and that instrumental smearing can decrease that gradient. In conclusion, the reader should be aware of this effect in velocity-resolved data, but we do not feel that it produces the entire trend seen in this dataset.

A potentially critical systematic effect is the wavelength or velocity calibration, since we combine data from different instruments. The FUSE wavelength calibration in older versions of the data pipeline in particular was uncertain at the 5–10 km s<sup>-1</sup> level. However, the alignment of low-ionization interstellar absorption lines with H I 21 cm emission can be used to correct the wavelength solution, at least in the neighborhood of the Li-like ions. The wavelength offset for all data was corrected in the same way. The wavelength offset was measured in low-ionization, narrow interstellar absorption lines expected to be present predominantly in neutral atomic gas: Si II, O I, C II, Ar I, Fe II, N I, and S II. These were aligned with the LSR velocity of the neutral hydrogen emission measured in the 21 cm line, either with the Leiden-Dwingeloo survey (Burton & Hartmann 1994) or the Parkes Multibeam survey (Haynes et al. 1999). We found the accuracy of this standard method of absolute wavelength calibration to be  $\lesssim 5$ –10 km s<sup>-1</sup>. Wakker et al. (2003) made extensive tests of this calibration and found a similar accuracy. They also noted that version 1.8.7 of the FUSE pipeline led to a 10 km s<sup>-1</sup> offset between O VI 1032 and O VI 1038. Further investigation by scientists involved with FUSE pipeline development (Kruk & Sembach 2002, private com-

munication) found that the earlier software did indeed introduce a stretch in the wavelength scale corresponding to 8 km s<sup>-1</sup> over the range spanned by the low-ionization lines used (post-pipeline) to correct the wavelength. (There was also an incorrect minus sign in the conversion from spacecraft to LSR velocity.) The correction as applied here did take into account that wavelength “stretch” when data quality allowed it to be measured. Further, several sample sightlines were re-reduced using version 2.0.5 of the FUSE pipeline, which has improved the “stretch” and wavelength calibration issues; no significantly different offsets between O VI and N V were discovered. Although these tests show no evidence of systematic wavelength calibration issues, we estimate the maximum systematic effect (due to remaining issues in the new pipeline or perverseness of the data) to be 5 km s<sup>-1</sup>, which would introduce an N V/O VI slope of 0.0014 dex (km s<sup>-1</sup>)<sup>-1</sup>, less than half of the mean effect seen in Figure 6. Thus, we believe it unlikely that the entire trend seen here is due to systematic problems in the FUSE calibration process, though we can only rule this out with 80% confidence. (There is a 20% chance that so many of our ion slopes would be negative if the true mean slope in the Galactic halo was zero.)

#### 4. Implications for the Galactic Distribution of Hot Gas

The Li-like ions C IV, N V, and O VI are produced in nonequilibrium physical situations, such as shocks, conductive interfaces and rapidly cooling gas (Paper I). The different ions are generally produced at different flow velocities in the structure, so

a viewer looking through such a structure will see trends in the ion column density ratios as a function of line-of-sight velocity. The ratio-velocity signature in all possibly relevant physical situations must be considered to properly interpret trends in the data.

Trends in the column density ratios, and those ratios as a function of line-of-sight velocity, could also reflect differences in the spatial distributions of the different ions in the Galactic halo. In the following sections we interpret our dataset in terms of the large-scale distribution of hot gas in the halo. We attempt (unsuccessfully) to model the observed trends in ion ratio with such a purely *kinematic* model, as opposed to the more physical models (shocks, conductive interfaces, etc) discussed in Paper I.

#### 4.1. Corotating Smooth Halo

As a reasonable starting point, one can imagine a smooth halo of ionized gas distributed in an exponential distribution in Galactic altitude, corotating on cylinders with the disk gas, without postulating a physical mechanism for producing this distribution. A smooth density distribution requires fewer assumptions than a patchy or clumpy one. There is observational evidence of such patchiness (for example the scatter in total column density and column density ratio found in this study, and the extensive investigation of Howk et al. (2002) showing large variations in O VI towards the Magellanic Clouds), but a smoothly distributed model may capture the averaged global characteristics of the gas. As for the second assumption, a rotation rate independent of Galactic altitude

is the simplest starting point, although observational evidence for such corotation is ambiguous. For example, Savage et al. (1997) argue that C IV corotates with the disk up to Galactic altitudes  $|z| \sim 5$  kpc, based on the lack of strong secondary absorption peaks. This is a well-known phenomenon in which strong velocity gradients along the line of sight can create discrete features in an absorption spectrum. These look like density enhancements, even if the true space density of the gas is smooth or constant. It is not clear that the lack of secondary features can be used in this manner to argue for corotating gas, or at least a small velocity gradient, if the halo gas distribution is extremely patchy. It is notable that there is significant C IV absorption visible in their figures outside of the velocity range allowed by corotation, and that there is somewhat more of this gas at negative than positive velocities. (The authors also note that 7/9 sightlines show negative C IV velocities, with similar results for N V). Significant forbidden-velocity gas was also detected near the Galactic center by Tripp et al. (1993). Even a fairly smooth halo in a rising fountain flow may not corotate with the disk; Bregman (1980) notes that the rotation speed decreases with altitude, mostly because the radial gradient in the Galactic gravitational potential decreases with altitude.

Despite the probable incompleteness of this model, it is instructive both to attempt to determine the scale height of the hot gas, and to model the ion-ratio signature that such a structure would have in velocity space.

## 4.2. Scale Heights

The scale height of the halo gas can be determined by fitting  $N|\sin(b)|$  versus Galactic altitude  $z$  (Savage et al. 1997, for N V, C IV, and Si IV). One obtains a scale height and midplane density from the fit. Naturally, when only extragalactic targets are observed, one takes the mean  $N|\sin(b)|$  and divides by a given midplane density to obtain the scale height, instead of obtaining the midplane density directly from the data. Figure 12 shows  $N|\sin(b)|$  for N V and O VI and the derived scale heights using midplane densities of  $n_0=1.7\times 10^{-8}\text{ cm}^{-3}$  (Jenkins 2001) for O VI and  $n_0=2.6\times 10^{-9}\text{ cm}^{-3}$  (Savage et al. 1997) for N V. The scale heights agree with previous work, confirming that the vertical extent of gas increases with decreasing ionization stage, from O VI to N V to C IV to Si IV. Such trends were predicted by Shull & Slavin (1994). The large variations in  $N|\sin(b)|$  result from the extreme patchiness of the gas in even large scales. Savage et al. (1997) used a patchiness parameter in their fits to the scale height, and found that almost all of the scatter is from intrinsic patchiness rather than observational random error. This is further confirmed by Savage (2001), who saw a hint that the O VI distribution cannot be fitted by a plane-parallel structure (or that there is large variation above different parts of the Galactic disk), and by Savage et al. (2003), in which patchiness is the clear cause of the data being consistent with scale heights 2–5 kpc. The extreme patchiness of interstellar hot gas is also confirmed by measurement of O VI emission – the ratio of emission (proportional to  $n^2$ ) to absorption (proportional to  $n$ ) gives

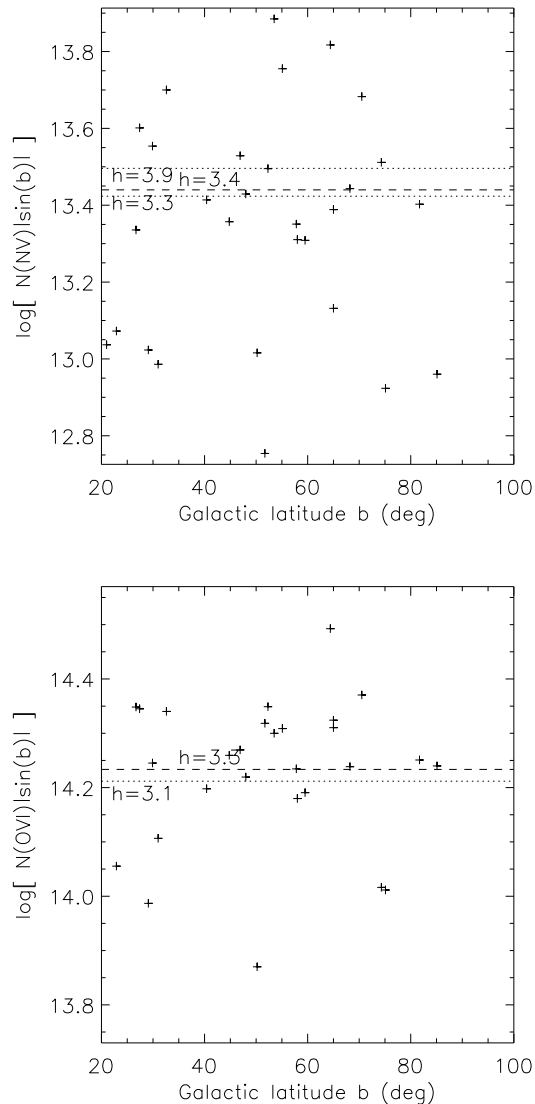


Fig. 12.— Scale heights in kpc for N V and O VI determined from  $N|\sin(b)|$ . The value determined here is marked with a dashed line, and the values determined previously are dotted (Savage et al. 1997, 2000a). For N V, Savage et al. (1997) determined a higher (lower) scale height depending on whether some of their upper limits were treated as measurements (or not). The value found here falls between their values. Only the highest signal-to-noise N V data (error in total  $N(\text{N V}) < 0.35$  dex) was used to calculate the N V scale height (although including all sightlines doesn't change the answer to within error).

the space density  $n$ , and shows that the gas is contained in small, dense structures, not a diffuse smooth distribution (Shelton et al. 2001; Dixon et al. 2001). This is expected since this gas is commonly produced in thin interfaces or highly disturbed cooling gas.

### 4.3. Deconvolution of observations

If one assumes that the hot halo gas corotates on cylinders with the disk, line-of-sight velocity can be mapped onto Galactic altitude  $z$  and Galactocentric radius  $R_G$ . This mapping does not reveal any trend of ion column density ratio with  $z$  in this dataset. This does not rule out a change in ionization as a function of Galactic altitude. It merely demonstrates that a simple mapping based on smoothly distributed gas corotating on cylinders above the disk is of limited use at high latitudes. Similarly, there is no clear trend in ion column density ratio as a function of implied Galactocentric radius  $R_G$ . This is even less surprising, as the sample here consists of mostly high-latitude sightlines. It is known that there is a gradient in Galactic metallicity, with a factor of 10 drop from Galactic center to the outer Galaxy, resulting from the gradient in star formation activity. There are suggestions, but no incontrovertible evidence, that the gradient might be steeper for nitrogen ( $-0.09 \pm 0.01$  dex  $\text{kpc}^{-1}$ , Rolleston et al. 2000) or carbon (Hou et al. 2000) than for oxygen ( $-0.067 \pm 0.008$  dex  $\text{kpc}^{-1}$ , Rolleston et al. 2000). The dataset presented here may show hints of decreasing  $\text{N(C IV)}/\text{N(O VI)}$  at larger  $R_G$ , consistent with a steeper gradient of carbon than oxygen, but the trend is not statistically significant. (The mean

$\text{N(C IV)}/\text{N(O VI)}$  decreases by less than 0.2 dex from  $R_G$  of 5 to 100 kpc while the variation along and between lines of sight is an order of magnitude). Even if this trend exists, it could indicate a change in ionization and not metallicity as a function of  $R_G$ . In this dataset, it is probably an artifact of trying to extract information from high-latitude sightlines with weak assumptions about corotation.

### 4.4. Modeled velocity-ionization signature

Mapping the data to Galactic altitude using corotation on cylinders is questionable and does not produce illuminating plots. It is more instructive to model what the velocity-ionization signature of a smoothly corotating halo would be, to better understand what observations could show. Figure 13 shows the modeled trend in  $\log[\text{N(N V)}/\text{N(O VI)}]$  as a function of line-of-sight velocity for sightlines at  $b=+40^\circ$  through a smooth, corotating halo in which the scale height of N V is larger than O VI (§ 4.2, Savage et al. 2000a, 1997). The thickness of the line scales with the density of N V and O VI at that point along the line of sight. This figure also shows the distribution of sightlines in this study. There is an excess of sightlines in the northern sky near  $l \sim 120^\circ$ , and this direction would display decreasing  $\text{N(N V)}/\text{N(O VI)}$  at more positive velocities in such a smooth halo. It should be recalled that these sightlines also pass through HVC Complex C, and might be expected to have special characteristics for that reason. However, no difference was detected in the column density ratio along these sightlines compared to the general



sample (Figure 7).

The velocity resolved ion ratio signature of a smoothly corotating halo is further illustrated in Figure 14, in which the predicted trend is shown as a function of Galactic longitude  $l$  and latitude  $b$ . The predicted slope is symmetric in  $b$  and antisymmetric in  $l$ , so only  $b > 0$  and  $0 < l < 180$  is shown. Also shown are the Galactic locations of the observed sightlines and their predicted slopes. There is no correlation between the observed and predicted slopes. Sembach et al. (2003) explore the possibility of fitting high velocity O VI with a corotating halo model and find that the data do not support (but also do not rule out) such an arrangement.

### 5. Conclusion and Summary

We consider the diagnostic power of velocity-resolved column density ratios in understanding the Galactic halo. Column density ratios of Li-like ions in the Galaxy are useful to diagnose the physical formation mechanism of the gas and to study the interstellar gas cycle, and a survey of these ions can reveal general trends. We find, in a survey of sightlines observed with FUSE and HST, that the distribution of  $N(\text{N V})$  and  $N(\text{O VI})$  in the halo does not appear to favor a dominant physical production mechanism. We find a possible weak trend of decreasing  $N(\text{N V})/N(\text{O VI})$  at more positive velocities ( $-0.0032 \pm 0.0022(r) \pm 0.0014(\text{sys}) \text{ dex (km s}^{-1})$  Figure 6). The weakness of this trend also argues against halo sightlines dominated by a single structure, e.g. the Local Bubble interface.

In Paper I we presented models of interfaces and cooling nonequilibrium gas,

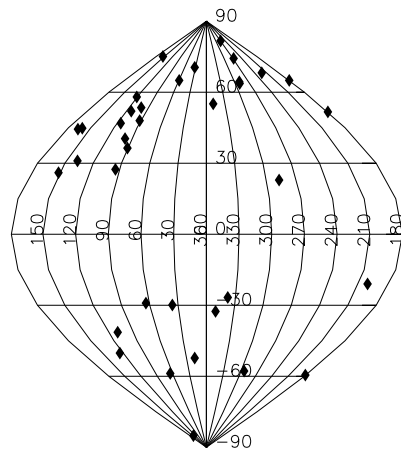
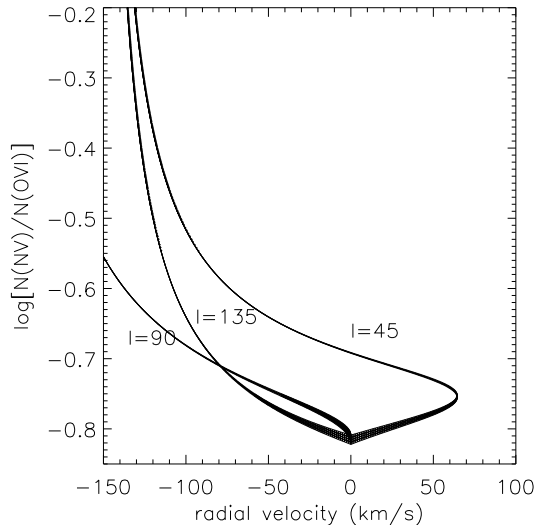


Fig. 13.— Signature of a smoothly corotating halo with different scale heights for N V and O VI. The left panel shows  $\log[N(\text{N V})/N(\text{O VI})]$  as a function of radial velocity for sightlines at  $b=40^\circ$  and various Galactic longitudes in the 1<sup>st</sup> and 2<sup>nd</sup> quadrants, for a smooth, corotating halo with a larger scale height of N V than O VI. The trend is reversed in velocity for sightlines in the 3<sup>rd</sup> and 4<sup>th</sup> quadrants, and reversed in the log of the column density ratio for southern sightlines. The right panel shows the distribution of sightlines in this study.

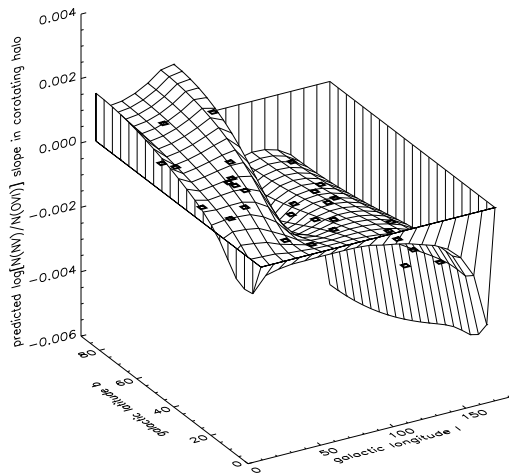


Fig. 14.— Predicted slopes in the log of the column density ratio  $N(\text{N V})/N(\text{O VI})$ , in a model in which the halo is corotating on cylinders with the disk, and there ions follow smooth exponential distributions in Galactic altitude  $z$  (different scale heights for each ion). The predicted ion slopes at the Galactic positions of the observed sightlines are marked.

and the velocity-resolved  $N(\text{N V})/N(\text{O VI})$  signatures of each. Here, we consider the model of smoothly distributed gas corotating on cylinders with the Galactic disk, and implications for the scale heights of  $\text{N V}$  and  $\text{O VI}$ . Observable velocity-ionization trends are weak, because even very strong trends are washed out by the large thermal width of the gas at different parts of the flow. Additional confusion results because the long sightlines almost definitely pass through multiple structures. In fact, the dispersion of  $N(\text{N V})/N(\text{O VI})$ , both integrated and velocity-resolved, clearly indicates that no single production scenario known to date can completely explain the Galactic halo. To truly understand the physical production of Li-like ions in the halo, one needs to analyze gas in localized areas of physical space, rather than velocity space. Absorption spectroscopy towards many halo stars with close angular separation and different distances could help to isolate gas at a specific altitude. Similarly, the gas above known superbubble shells or chimneys could be isolated. These observations have a greater chance of distinguishing between models of hot gas production than observations along long lines of sight.

We thank S. Penton, E. Wilkinson, J. Green, B. Savage, and K. Sembach for useful discussions. We thank the referee for a thorough reading of the manuscript. R.I. was partially supported during this investigation by an NSF Graduate Student Fellowship to the University of Colorado. J.M.S. acknowledges support from NASA grant NAG5-7262 and NSF grant AST02-06042. This work was based in

part on data obtained for the Guaranteed Time Team team by the NASA-CNES-CSA FUSE mission operated by the Johns Hopkins University. Financial support to U.S. participants has been provided by NASA contract NAS5-32985. We thank the members of the FUSE instrument, science, and operations teams for their dedicated efforts. We also thank the FUSE science team and the principal investigators of the STIS and GHRs observations for their permission to use these data, in some cases before public release.

## A. Notes on individual sightlines

Some of the sightlines have previously published analyses, and some pass through Galactic structures or high velocity cloud structures of particular interest (see Figure 13 for a plot of the sightlines in Galactic coordinates). The sightlines in this study were each examined in the light of previous analyses to determine if they had special characteristics warranting exclusion from a general study, or if there were any discrepancies with previous measurements. No instances of either were found. Figures 24–31 show selected examples of the velocity-resolved column densities.

Sightlines without notable Galactic interstellar features or data characteristics are not discussed here. One of the most obvious differences between sightlines is whether they pass through Galactic radio loops, which are probably superbubble shells filled with hot gas. Although these sightlines have typically higher total column densities of Li-like ions than other sightlines, it is logical to keep them in the sample for this study, because the tops of superbubbles and the hot gas and shells that comprise them make up the Galactic fountain flow. Sightlines that pass through radio loops might preferentially sample rising material from the fragmented tops of superbubbles, and other sightlines might preferentially sample more evolved cooling gas returning to the disk, but our understanding of the Galactic fountain is not precise enough to justify any culling of our sample of halo sightlines.

**3C273:** The sightline towards the bright quasar 3C273 was described in some detail by Savage et al. (1993a). It passes through radio continuum Loops I and IV (Berkhuijsen et al. 1971) and the North Polar Spur (Heiles et al. 1980; Snowden et al. 1995). Galactic radio loops in general, and Loops I and IV in particular (Iwan 1980), are believed to be supernova remnants or superbubbles filled with hot gas, so this sightline is expected to be strongly influenced by the interface between that hot gas and the denser shell around it. Savage et al. (1993a) note that the high-ionization lines have average velocities  $\sim 10 \text{ km s}^{-1}$  more negative than weaker-ionization lines, which they attribute to infalling hot gas. From analysis of low-ionization lines, Sembach et al. (2001b) find elemental depletions typical of warm diffuse halo clouds, consistent with a partial destruction of grains (stripped mantles with cores remaining). They also note that C IV, N V, and O VI have similar absorption profiles except for a high positive-velocity wing of O VI, which they attribute to hot gas being expelled from the Galaxy.

Despite the presence of the radio loops, there was no compelling reason to exclude the 3C273 sightline from the general analysis of this study. (In particular, the proposals of other authors that this sightline is involved with hot gas flowing in or out argues for its inclusion in this study of halo gas dynamics.) The resolved N V/O VI and C IV/O VI ratios found here agree well with the integrated ratios of Sembach et al. (2001b), as does the integrated O VI column density. The integrated N V column density agrees well with that of Penton et al. (2000b).

**3C351:** The sightline to this quasar passes through HVC Complex C, the edge of Galactic radio Loop III, and through the outer warp of the Galaxy (Savage et al. 1993b). Absorption

associated with the outer warp or with Complex C (these two structures may join or be related, see Wakker & van Woerden 1991) is seen at similar velocities as in H1821+643, but the FUSE data are of insufficient quality for detailed analysis. This sightline is therefore excluded from the sample used to search for general trends.

**ESO141-G55:** The sightline towards ESO141-G55 passes near the inner Galaxy and through the edge of radio Loop II. Sembach et al. (1999) and Shull et al. (2000) note the presence of fairly cold molecular gas, suggesting denser intervening material than other sightlines of similar Galactic latitude, and possibly related to some enhancement of Li-like ions relative to nearby lines of sight. The ion ratios found here are consistent with their integrated values, and no striking high velocity absorption is noted.

**Fairall 9:** The Fairall 9 sightline passes through the Magellanic Stream, which accounts for positive velocity absorption in the Li-like ions. The apparently higher column densities reported here compared to Savage et al. (1997) are the result of not distinguishing between the Galactic and Magellanic Stream components. The numbers found here for just the disk component agree with theirs. The two components are separated in velocity for C IV, and possibly for O VI, but are difficult to distinguish in N V (indeed the N V detection is very weak, and only the Galactic absorption was used in analysis of ion ratios). The large linewidths do not allow separation of different MS high velocity clouds (HVCs) seen at 160 and 200 km s<sup>-1</sup> in 21 cm emission (Morras 1983). The column density ratio  $\log[N(\text{N V})/N(\text{O VI})]$  has a lower limit of  $-1.7$  in the high-velocity MS absorption, and  $\log[N(\text{C IV})/N(\text{O VI})]$  ranges from  $-0.5$  to  $-0.9$ . These values are lower than typical for gas believed to be part of the Galactic halo and probably indicate a higher ionization state. Lu et al. (1994) find little evidence of depletion in the MS, which would lower C IV/O VI but probably not N V/O VI.

**H1821+643:** The sightline to this quasar passes through the warp of the outer Galaxy, seen in lower ionization species and C IV at  $v < -100$  km s<sup>-1</sup> (Savage et al. 1993b). The sightline also passes near the HVC Complex C, and through the edge of radio Loop III. Savage et al. (1995) note that the sightline passes near planetary nebula K1-16, but probably not near enough to contribute to the N V and C IV absorption. Savage et al. (2003) claim however that the planetary nebula does contribute to O VI. Savage et al. (1995) suggest that the bulk of the absorption, near 0 km s<sup>-1</sup> LSR velocity, may be associated with the Loop III superbubble. They argue that the absorbing gas is hot based on the large line widths and low C IV/N V ratio, which is consistent with collisional ionization equilibrium. This is confirmed by an anomalously high ratio  $\log[N(\text{N V})/N(\text{O VI})] \sim -0.1$  observed here. The C IV/O VI and N V/O VI ratios found here are also consistent with collisional ionization equilibrium (in contrast to almost all of the other gas observed in this project), and in particular the high N V/O VI and C IV/O VI ratios imply a temperature of  $T \simeq 10^{5.3}$  K. Savage et al. (1995) could not distinguish between that temperature and a higher one ( $6\text{--}10 \times 10^5$  K) based on their single ion ratio.

Absorption is detected in all 3 lines near  $-100$  km s<sup>-1</sup>, with somewhat low N V/O VI and C IV/O VI column density ratios; this is consistent with somewhat higher ionization state

in the more extended gas of the warp, but the gradient in ion ratio is not significant enough to make a definitive claim. Savage et al. (1995) argued that this gas, which they observed primarily in C IV, is not related to the Galactic fountain because the supernova rate and energy to drive the fountain are low in the outer Galaxy. They go on to propose that the gas could be photoionized. However, detection of O VI at similar velocities in this study and by Oegerle et al. (2000b) argues for a collisional ionization origin of the gas, and is thus left in the general sample of this study. Absorption detected near  $-200 \text{ km s}^{-1}$  may be associated with Complex C, but the ion column density ratios are not significantly deviant from average halo values, and is more likely associated with the maximum velocity allowed by the distant Galactic warp gas. (This gas was also noted in O VI absorption by Oegerle et al. 2000b)

**Markarian 110:** The sightline to this Seyfert galaxy lies just off the edge of HVC Complex A, and just outside of Galactic radio Loop III. This sightline was excluded from the analysis because of the low quality of the FUSE data and the questionable N V detection, although the sightline is probably acceptable for halo study with better data.

**Markarian 116:** (I Zwicky 18) This sightline pierces high velocity cloud Complex A and a marginal detection of N V at  $v \sim -150 \text{ km s}^{-1}$  might be associated, but this is rejected as is the entire sightline, because no low-velocity N V is detected.

**Markarian 279:** The sightline to this Seyfert I galaxy passes through HVC Complex C and the edge of radio Loop III. Extended negative velocity absorption  $\lesssim -100 \text{ km s}^{-1}$  seen in N V and O VI could either be Galactic halo gas at velocities permitted by the rotation curve or could be associated with the HVC. As there is no clear separation of the absorption into components, the entire velocity range is kept in the sample. Penton et al. (2000b) suggested that the N V  $\lambda 1239$  line might be intergalactic Ly $\alpha$ , but because the  $\lambda 1242$  is definitely confused with intergalactic absorption this identification can neither be confirmed nor denied, and it is assumed to be N V here. No indication that the radio Loop is accounting for atypical conditions is evident in these observations.

**Markarian 290:** This sightline also passes through HVC Complex C, but probably misses radio Loop III. The FUSE data are only of modest quality, but gas is clearly detected in N V and O VI. The column density ratio N V/O VI shows a large variation in the high velocity ( $v \sim -100 \text{ km s}^{-1}$ ) gas, but the error bars are large. Complex C was reported detected in Ca II along this sightline, at  $v = -137 \text{ km s}^{-1}$  (Wakker & van Woerden 1997), close to the same velocity as the N V and O VI absorption.

**Markarian 335:** This sightline just misses the tail of the Magellanic Stream and passes through the center of Galactic radio Loop II. There is O VI at large negative velocities which could be associated with the MS ( $-350 < v < -150 \text{ km s}^{-1}$ ). N V absorption is extremely weak, and although there is the hint of a very low N V/O VI ratio in both the low and high velocity gas, the ratio could not be determined well enough to include in the sample.

**Markarian 421:** The closest HVC to this BL Lac sightline is Complex M, several degrees away. N V column densities are low but not undetected.

**Markarian 509:** Savage et al. (1997) report total (low-velocity) N V and C IV column

densities towards Mkn 509 consistent with those found here, and the ion ratios agree with those reported by Sembach et al. (2001b). This sightline is particularly interesting because of the detection of highly ionized high velocity gas, undetected in neutral hydrogen; Sembach et al. (1995) see C IV at  $-340 < v < -170$  km s<sup>-1</sup> and no H I emission at those velocities (though there is H I emission at similar velocities 1-2 degrees away). They only place an upper limit on N V, and argue that the clouds may be photoionized because conductive interface and cooling gas models have difficulty producing the large ratios C IV/N V  $\gtrsim 5$  they observe. Photoionization does require the clouds to be large (at least a kiloparsec). In this dataset, high velocity gas is observed in O VI as well as C IV, and again the N V detection is marginal at best. The presence of O VI tends to argue against photoionization, because photoionization leads to unreasonably large cloud sizes if the absorbers are associated with our Galactic halo. An ionization parameter  $U = n_\gamma/n_H \gtrsim 10^{-1}$  would be required to produce the observed column density ratio  $\log[N(\text{N V})/N(\text{O VI})] \lesssim -1$  via photoionization by the extragalactic background of quasars and AGN (Tripp & Savage 2000). This translates into a density upper limit  $\log(n_H) \lesssim -5.5$ ,  $\log(n_{\text{OVI}}) \lesssim -9$ , and the observed O VI column density yields a physical cloud size of  $R \gtrsim 100$  kpc (although the O VI absorption is confused with molecular hydrogen, assuming the maximum  $2\sigma$  allowed H<sub>2</sub> column from other H<sub>2</sub> lines still leaves  $N(\text{O VI}) \gtrsim 1.2 \times 10^{14}$  cm<sup>-2</sup>). Finally, it is not clear that similar C IV and O VI column densities can be reconciled with very low N V in a purely photoionization model. The three ions are still consistent with turbulent mixing layer models (also noted by Savage et al. 1997) but large numbers of such interfaces would be required to produce the total column densities.

**Markarian 817:** The sightline passes through HVC complex C. As with the other sightlines in this part of the sky, it is not possible to determine whether the gas seen at negative velocities is part of the extended disk or the high velocity cloud.

**Markarian 876:** This sightline represents the first detection of O VI in a high velocity cloud, namely Complex C (Murphy et al. 2000). Unfortunately the N V absorption is only marginally detected in the high velocity gas. The ion ratio in the high velocity gas is  $\log[N(\text{N V})/N(\text{O VI})] \sim -0.8$  in the HVC, not significantly different from the range in the low velocity gas along this sightline or in the halo in general.

**Markarian 926:** This sightline just misses the tail end of the Magellanic Stream, but does pass through Galactic radio Loop III. The FUSE data was of insufficient quality to include this sightline in further analysis.

**Markarian 1383:** This sightline passes through Loop I and near Loop IV. No unusual gas is detected in the line profiles or ion ratios.

**Markarian 1502:** (I Zwicky 1) The sightline to this narrow-line quasar passes through the center of radio Loop II. Absorption seen near 1031 Å is probably highly contaminated by molecular hydrogen, which is present along this sightline (although the modest signal-to-noise does not permit a very accurate determination of the column density), so only the low-velocity gas detected in O VI and N V is analyzed. The N V/O VI ratio is fairly high ( $\log[N(\text{N V})/N(\text{O VI})] \sim -0.6$ ) but has large error bars, so the difference does not merit

special treatment of the sightline.

**Markarian 1513:** (II Zwicky 136) This sightline passes through Galactic radio Loop II, but no anomalies are detected in the column densities profiles or their ratio.

**NGC 3783:** The sightline to the nucleus of this Seyfert I galaxy passes through the interior of Loop I and through the HVC 287.5+22.5+240. Sembach et al. (2001a) report on the FUSE observations of this high velocity gas and argue that it is the leading edge of the Magellanic Stream. As they point out, any O VI absorption in the high velocity gas (high positive or negative velocities) is obscured by intrinsic Ly $\beta$  absorption: NGC 3783 has a redshift of  $2929 \pm 3$  km s $^{-1}$  (Theureau et al. 1998) and prominent absorbers at  $-560$  and  $-1420$  km s $^{-1}$  (Crenshaw et al. 1999). The current data show no definite C IV or N V absorption at  $|v| \gtrsim 100$  km s $^{-1}$ , strengthening the claim that little of the observed absorption near 1031 Å is O VI.

**NGC 4151:** The sightline towards this nearly Seyfert I galaxy does not traverse any significant Galactic features, but isolation of the Galactic absorption does require some care because of absorption intrinsic to that galaxy. NGC 4151 has a variable outflow of hot gas (including absorption by the Li-like ions) at 0 to 1600 km s $^{-1}$  (the Seyfert has a redshift of  $\simeq 1000$  km s $^{-1}$ , Weymann et al. 1997). Weymann et al. (1997) fit the Galactic absorption from C IV together with the intrinsic, while our study treats the broad intrinsic absorption as a complex continuum. Comparison of the results suggests that the Galactic C IV absorption reported here is an underestimate because of the line-blanketing effect of intrinsic absorption. The line ratios N V/O VI and C IV/O VI found here are not particularly different from the halo mean.

**NGC 5548:** The integrated values for N V and C IV column densities are in agreement with Savage et al. (1997) along the unremarkable sightline towards this Seyfert I galaxy.

**PG0804+761:** The sightline towards this low-redshift quasar passes through the center of radio Loop III, very near high velocity cloud Complex A, and over the outer Galaxy spiral arms. Although there is O VI emission at moderately high velocities, there is none at  $-180$  km s $^{-1}$ , where Complex A gas would be expected (Richter et al. 2001a). The N V absorption at that velocity is obscured by what appears to be intergalactic Ly $\alpha$  absorption. At lower velocities (data in the wings of the Ly $\alpha$  absorber is discarded) the N V is weak but present. There is a break in the N V/O VI ratio near  $-40$  km s $^{-1}$  which might indicate a different ratio in low halo gas compared to the low-latitude Intermediate-Velocity Arch (see Richter et al. 2001a, for further description of the intermediate-velocity gas along this sightline.)

**PG0953+414:** The nearest high-velocity gas to the sightline towards this low-redshift QSO is  $1.7^\circ$  away at  $-91$  km s $^{-1}$  (Savage et al. 2000b). No anomalies are detected.

**PG1116+215:** Although there is no apparent H I high-velocity gas near the sightline towards this low-redshift quasar, Tripp et al. (1998) and Savage et al. (2000b) detect absorption from modestly ionized species (Si II, Mg II, C II, Si IV) at  $v \sim 200$  km s $^{-1}$ . The detection is confirmed here in the Li-like ions, with ion ratios  $\log[N(\text{N V})/N(\text{O VI})] \sim -0.7$



and  $\log[N(\text{N V})/N(\text{O VI})] \sim -0.1$ .

**PG1259+593:** The sightline to the quasar PG1259+593 passes through the Intermediate-Velocity (IV) Arch ( $-55 \text{ km s}^{-1}$ ), and high-velocity cloud Complex C ( $-130 \text{ km s}^{-1}$ ). The detection of O VI in these features reported by Richter et al. (2001b) is confirmed here, as well as marginal detection of N V with  $\log[N(\text{N V})/N(\text{O VI})] \sim -0.9$ . Savage et al. (1993b) note negative extensions of the absorption from C IV and lower ions which may be associated with IV gas, but the Faint Object Spectrograph resolution is insufficient to properly resolve components.

**PG1351+640:** The sightline towards this broad-absorption-line QSO passes through the high velocity cloud Complex C, but the FUSE data quality is insufficient to accurately study the Galactic absorption (see Zheng et al. 2001, for analysis of the intrinsic absorbers in the FUSE spectrum).

**PKS 2155-304:** The sightline to this BL Lac does not pass through any apparent high velocity gas detected in H I emission, but it does show high velocity absorption in O VI, C IV, Si IV, and certain low ions (Collins et al. 2004). Although these HVCs have been attributed to gas in the Local Group, the presence of the low ions (S II, C II) is more consistent with higher-density gas in the Galactic halo. Integrated column densities for the low-velocity halo gas agree with Savage et al. (1997) (N V and C IV) and Sembach et al. (2001b) (N V/O VI and C IV/O VI; the value for the latter is  $\sim 1\sigma$  higher than their value). The N V  $\lambda 1239$  line is a questionable identification; the above two papers associate it with Galactic N V, but Shull et al. (1998) associate it with intergalactic Ly $\alpha$  because of the weakness of the 1242 Å line. Because N V  $\lambda 1242$  is quite weak, we exclude this sightline from general analysis of the N(N V)/N(O VI) line ratio as a function of velocity.

**RXJ 1230.8+0115:** Like the sightline towards 3C273, this sightline passes through the edges of radio Loops I and IV. The sightline is not usable for general analysis because the O VI line is obscured by intergalactic Ly $\beta$ .

**TON S180:** This sightline lies about  $10^\circ$  off of the Magellanic Stream, and O VI has been previously detected at both high positive and negative velocities (Sembach et al. 2000). The positive velocity gas is not detected in N V, and although there is a hint of the negative-velocity gas, it is obscured by what is apparently intergalactic Ly $\alpha$  absorption.

**VII Zwicky 118:** This sightline passes through the center of ratio Loop III, but no anomalies are detected in the column densities profiles of O VI and C IV. Signal-to-noise is too low for N V to include in ratio analysis.

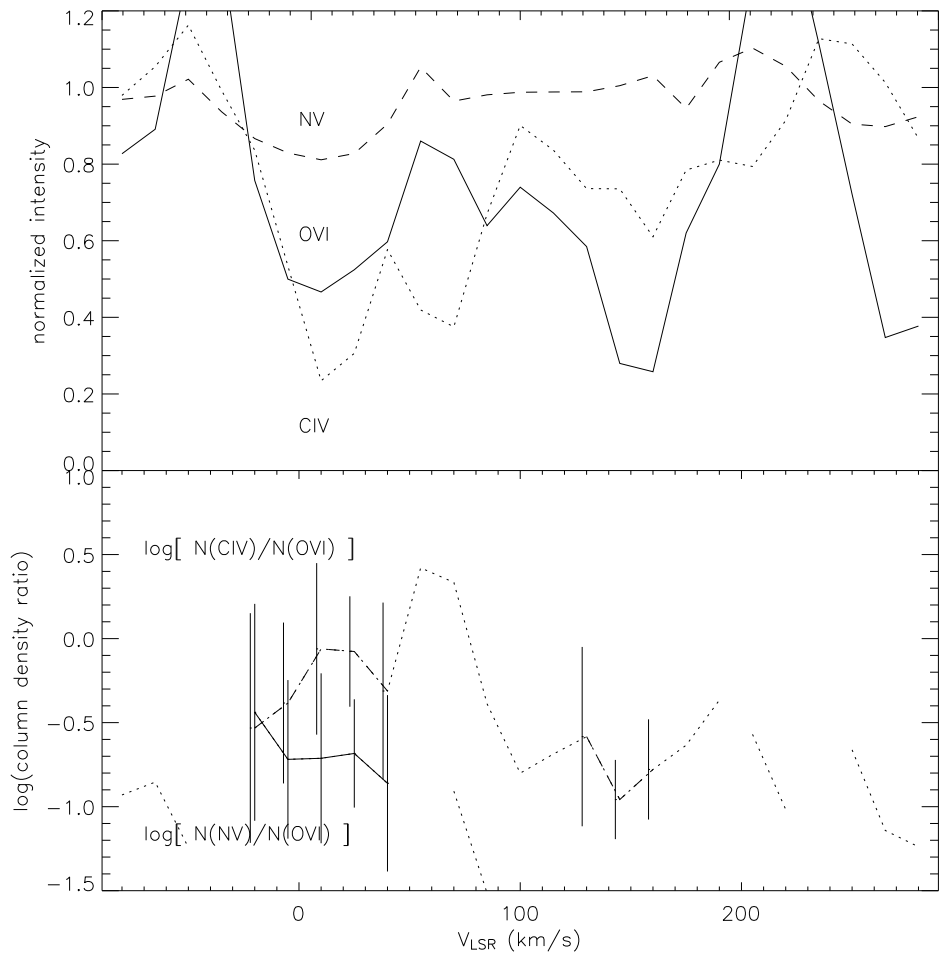


Fig. 15.— Fairall 9. Lines as in Figure 1.

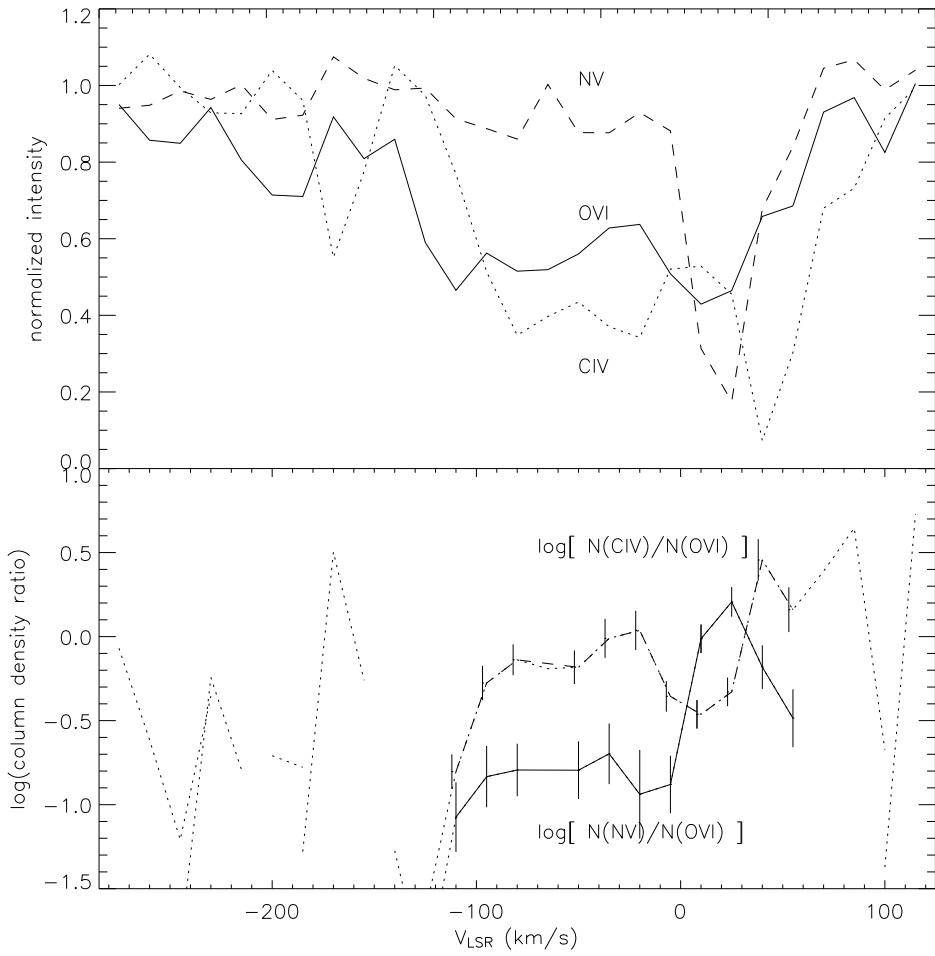


Fig. 16.— H1821+643. Lines as in Figure 1.

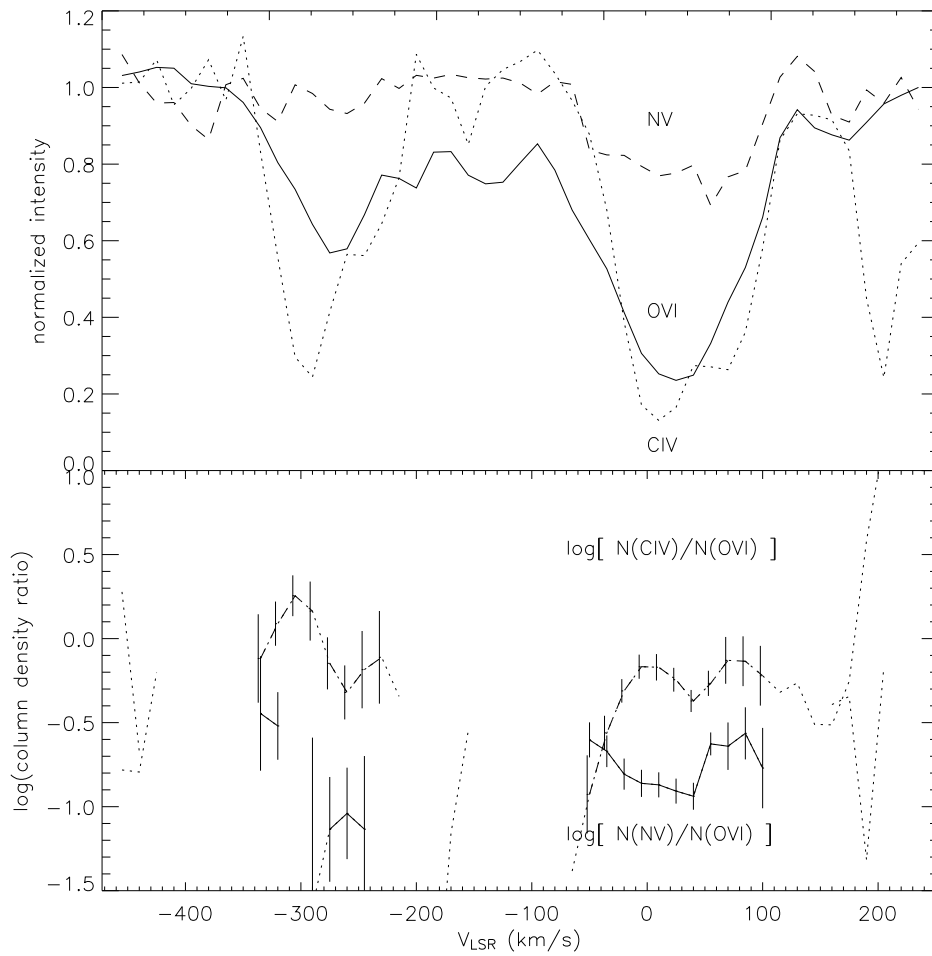


Fig. 17.— Markarian 509. Lines as in Figure 1.

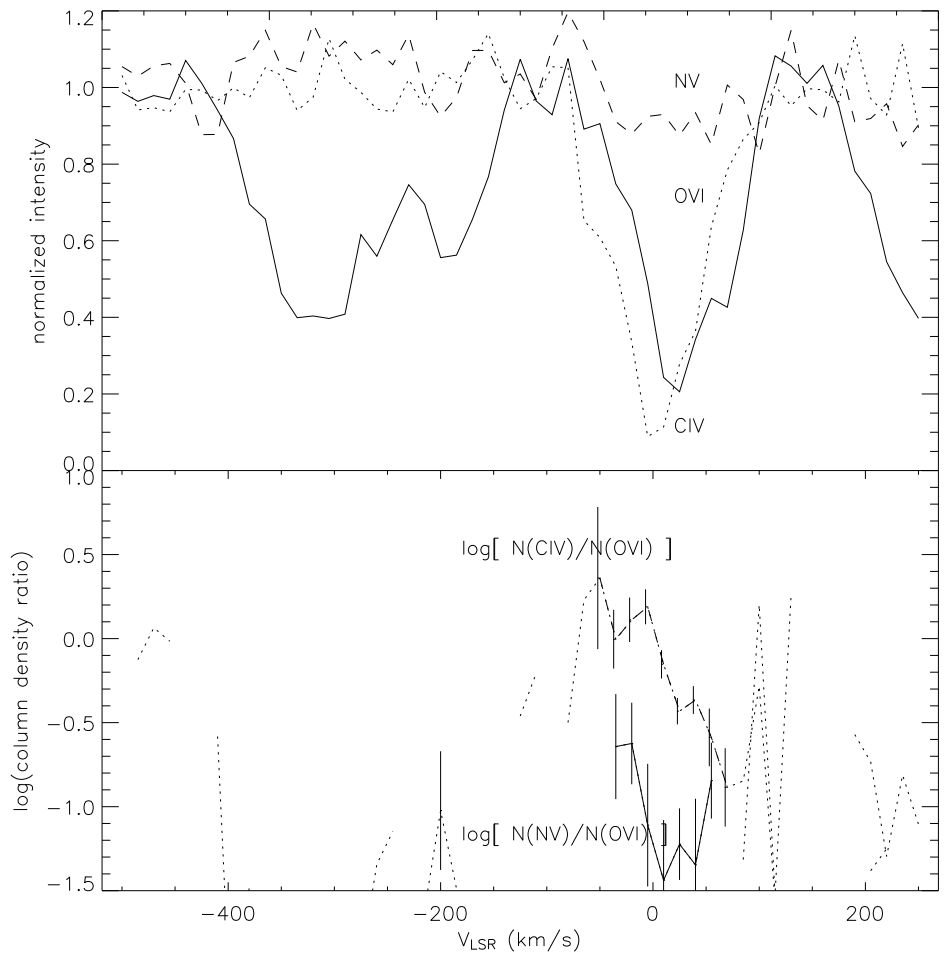


Fig. 18.— NGC3783. Lines as in Figure 1.

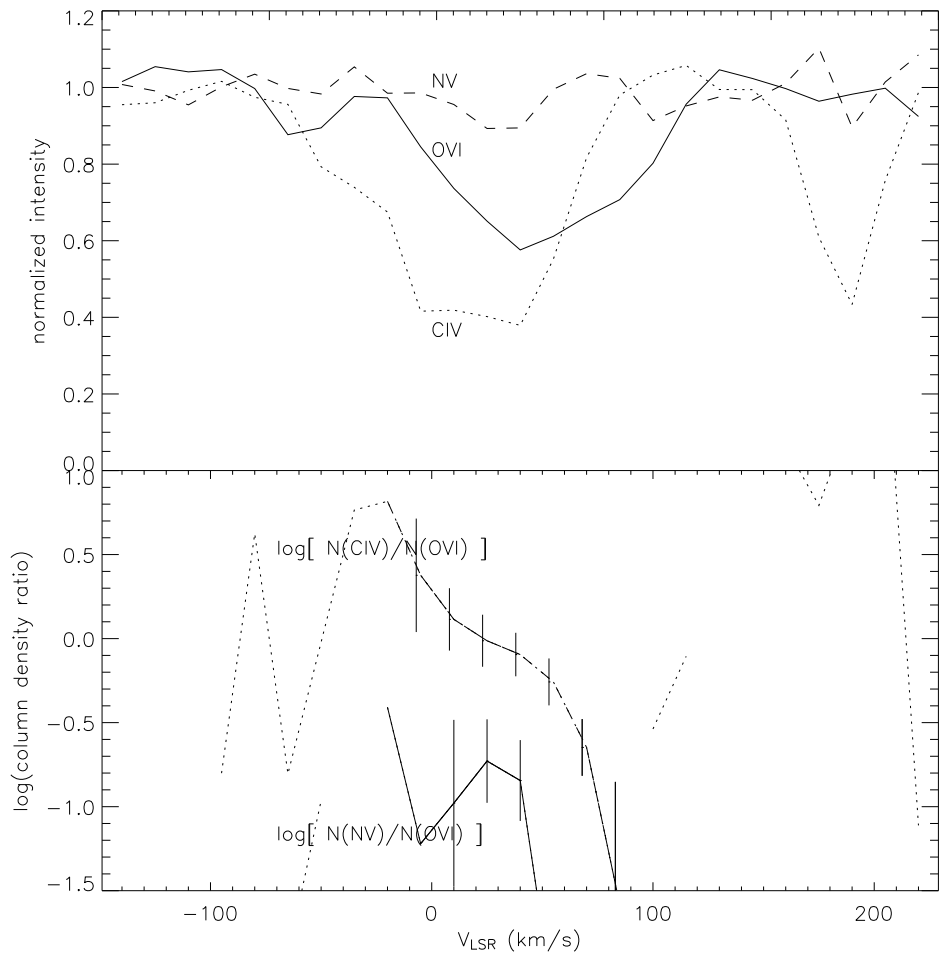


Fig. 19.— NGC4151. Lines as in Figure 1.

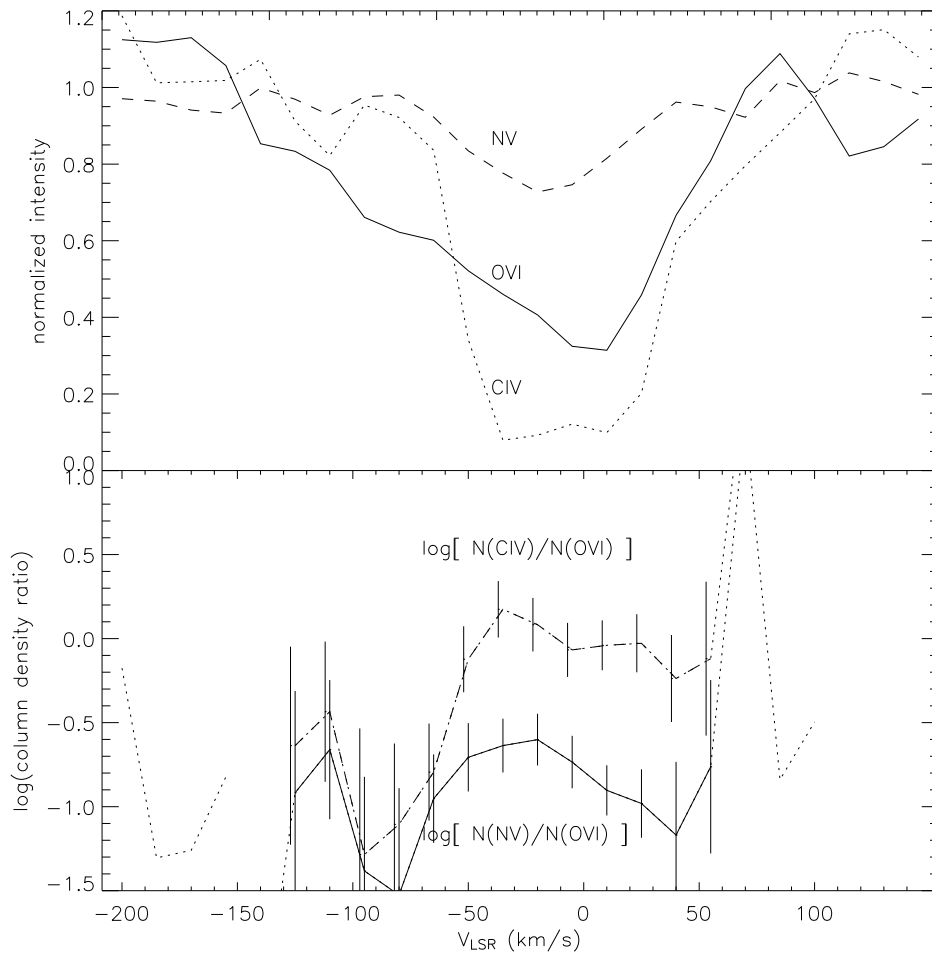


Fig. 20.— NGC5548. Lines as in Figure 1.

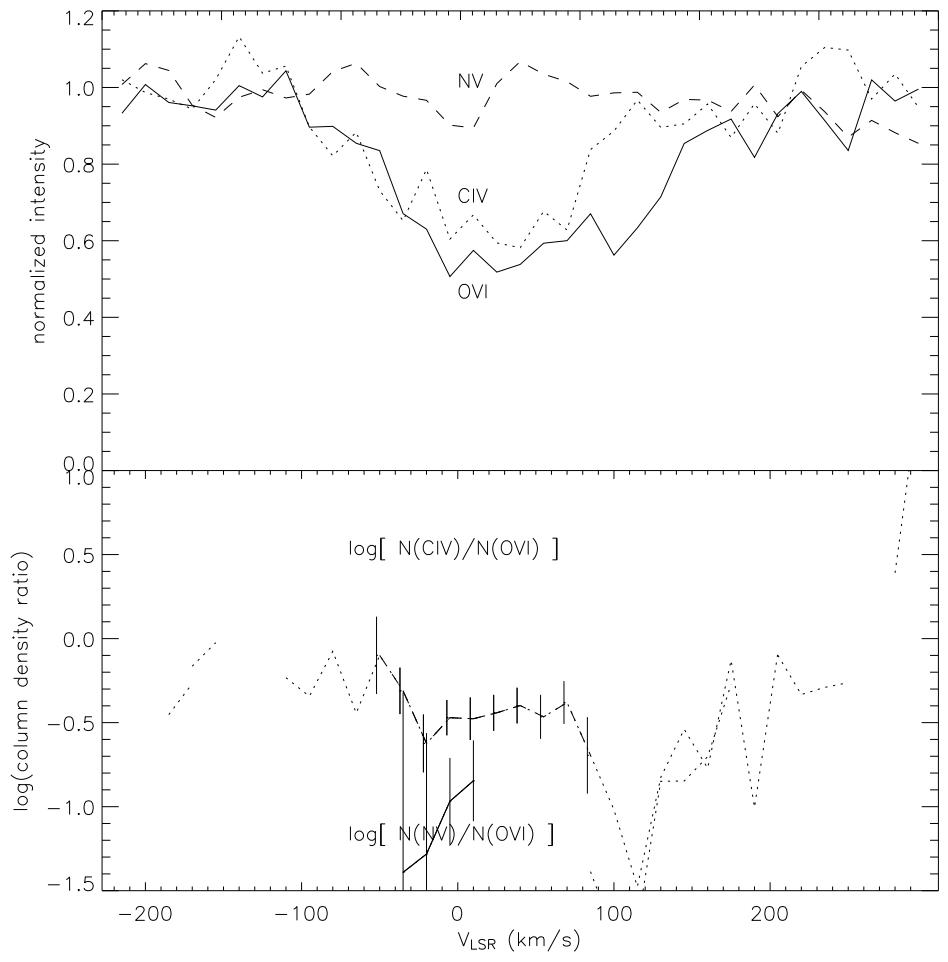


Fig. 21.— PG0953+414. Lines as in Figure 1.



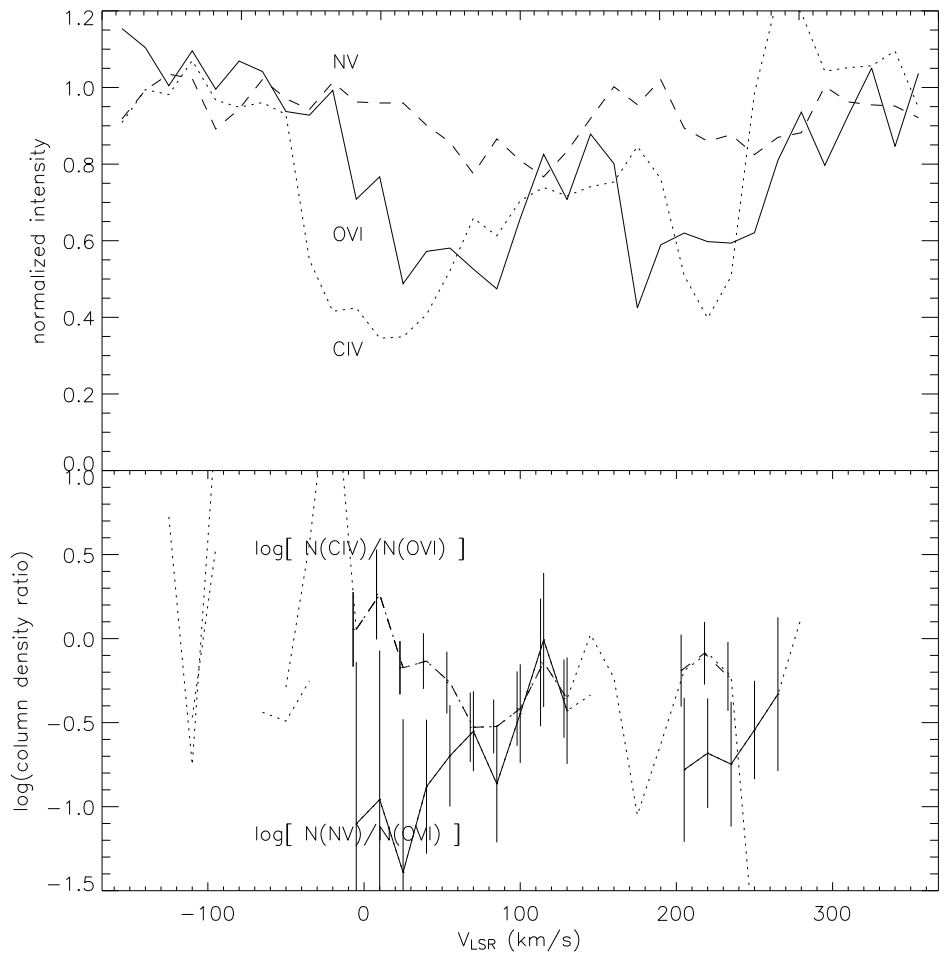


Fig. 22.— PG1116+215. Lines as in Figure 1.

## REFERENCES

- Benjamin, R., & Shapiro, P. 1993, in *Ultraviolet and X-ray Spectroscopy of Laboratory and Astrophysical Plasmas*, ed. E. Silver & S. Kahn (New York: Cambridge Univ. Press), 280
- Berkhuijsen, E. M., Haslam, C. G. T., & Salter, C. J. 1971, *A&A*, 14, 252
- Böhringer, H., & Hartquist, T. W. 1987, *MNRAS*, 228, 915
- Borkowski, K. J., Balbus, S. A., & Fristrom, C. C. 1990, *ApJ*, 355, 501
- Brandt, J. C., et al. 1994, *PASP*, 106, 890
- Bregman, J. N. 1980, *ApJ*, 236, 577
- Burton, W. B., & Hartmann, D. 1994, in *ASP Conference Series, Vol. 67, Unveiling large-scale structures behind the Milky Way*, ed. C. Balkowski R. C. Kraan-Korteweg, 31
- Collins, J., Shull, J. M., & Giroux, M. L. 2003, *ApJ*, 585, 336
- Collins, J., Shull, J. M., & Giroux, M. L. 2004, *ApJ*, 605, in press
- Crenshaw, D. M., Kraemer, S. B., Boggess, A., Maran, S. P., Mushotzky, R. F., & Wu, C. 1999, *ApJ*, 516, 750
- Davies, J., et al. 2001, *STIS Instrument Handbook*, available electronically from <http://www.stsci.edu/cgi-bin/stis?cat=documents&subcat=ihb>
- Dixon, W. V. D., Sallmen, S., Hurwitz, M., & Lieu, R. 2001, *ApJ*, 552, L69
- Gibson, B. K., Giroux, M. L., Penton, S. V., Stocke, J. T., Shull, J. M., & Tumlinson, J. 2001, *AJ*, 122, 3280
- Haynes, R., et al. 1999, in *New Views of the Magellanic Clouds*, ed. Y.-H. Chu et al., ASP, San Francisco, 63
- Heiles, C., Chu, Y., Troland, T. H., Reynolds, R. J., & Yegingil, I. 1980, *ApJ*, 242, 533
- Hou, J. L., Prantzos, N., & Boissier, S. 2000, *A&A*, 362, 921
- Howk, J. C., Savage, B. D., Sembach, K. R., & Hoopes, C. G. 2002, *ApJ*, 572, 264
- Indebetouw, R., & Shull, J. M. 2004, *ApJ*, 605, in press (Paper I)
- Iwan, D. 1980, *ApJ*, 239, 316
- Jenkins, E. 2001, in *Gaseous Matter in Interstellar and Intergalactic Space*, IAP Colloquium 17, ed. R. Ferlet, M. Lemoine, J.-M. Desert, B. Raban, (Paris: Frontier Group), 99
- Jenkins, E. B. 1996, *ApJ*, 471, 292
- Kimble, R. A., et al. 1998, *ApJ*, 492, L83
- Lu, L., Savage, B. D., & Sembach, K. R. 1994, *ApJ*, 437, L119
- Moos, H. W., et al. 2000, *ApJ*, 538, L1
- Morras, R. 1983, *AJ*, 88, 62
- Murphy, E. M., et al. 2000, *ApJ*, 538, L35
- Oegerle, W. R., Murphy, E., & Kriss, J. 2000a, *The FUSE Data Handbook*, available electronically from <http://fuse.pha.jhu.edu/analysis/dhbook.html>
- Oegerle, W. R. et al. 2000b, *ApJ*, 538, L23
- Penton, S. V., Shull, J. M., & Stocke, J. T. 2000a, *ApJ*, 544, 150
- Penton, S. V., Stocke, J. T., & Shull, J. M. 2000b, *ApJS*, 130, 121
- . 2004, *ApJS*, 132, in press
- Richter, P., Savage, B. D., Wakker, B. P., Sembach, K. R., & Kalberla, P. M. W. 2001a, *ApJ*, 549, 281
- Richter, P., et al. 2001b, *ApJ*, 559, 318
- Rolleston, W. R. J., Smartt, S. J., Dufton, P. L., & Ryans, R. S. I. 2000, *A&A*, 363, 537
- Sahnow, D. J., et al. 2000, *ApJ*, 538, L7
- Savage, B. 2001, in *Gaseous Matter in Interstellar and Intergalactic Space*, IAP Colloquium 17, ed. R. Ferlet, M. Lemoine, J.-M. Desert, B. Raban, (Paris: Frontier Group), 109
- Savage, B. D., Lu, L., Weymann, R. J., Morris, S. L., & Gilliland, R. L. 1993a, *ApJ*, 404, 124
- Savage, B. D., & Sembach, K. R. 1991, *ApJ*, 379, 245

- Savage, B. D., Sembach, K. R., & Lu, L. 1995, *ApJ*, 449, 145
- . 1997, *AJ*, 113, 2158
- Savage, B. D., et al. 1993b, *ApJ*, 413, 116
- . 2000a, *ApJ*, 538, L27
- . 2000b, *ApJS*, 129, 563
- Savage, B. D., et al. 2003, *ApJS*, 146, 125
- Sembach, K. R., Howk, J. C., Savage, B. D., & Shull, J. M. 2001a, *AJ*, 121, 992
- Sembach, K. R., Howk, J. C., Savage, B. D., Shull, J. M., & Oegerle, W. R. 2001b, *ApJ*, 561, 573
- Sembach, K. R., & Savage, B. D. 1992, *ApJS*, 83, 147
- Sembach, K. R., Savage, B. D., & Hurwitz, M. 1999, *ApJ*, 524, 98
- Sembach, K. R., Savage, B. D., Lu, L., & Murphy, E. M. 1995, *ApJ*, 451, 616
- Sembach, K. R., et al. 2000, *ApJ*, 538, L31
- Sembach, K. R., et al. 2003, *ApJS*, 146, 165
- Shapiro, P., & Benjamin, R. 1993, in *Star Formation, Galaxies and the Interstellar Medium*, ed. J. Franco, F. Ferrini, G. Tenorio-Tagle (New York: Cambridge Univ. Press), 275
- Shelton, R. L., et al. 2001, *ApJ*, 560, 730
- Shelton, R. L. 1998, *ApJ*, 504, 785
- Shull, J. M., Penton, S. V., Stocke, J. T., Giroux, M. L., van Gorkom, J. H., Lee, Y. H., & Carilli, C. 1998, *AJ*, 116, 2094
- Shull, J. M., & Slavin, J. D. 1994, *ApJ*, 427, 784
- Shull, J. M., et al. 2000, *ApJ*, 538, L73
- Slavin, J. D., & Cox, D. P. 1993, *ApJ*, 417, 187.
- Slavin, J. D., Shull, J. M., & Begelman, M. C. 1993, *ApJ*, 407, 83
- Snowden, S. L., et al. 1995, *ApJ*, 454, 643
- Soderblom, D., Gonnella, A., Hulbert, S., Leitherer, C., Schultz, A., & Sherbert, L. 1995, *GHRs Instrument Handbook*, available electronically from [http://www.stsci.edu/instrument-news/handbooks/ghrs/GHRs\\_1.html](http://www.stsci.edu/instrument-news/handbooks/ghrs/GHRs_1.html)
- Sutherland, R. S., & Dopita, M. A. 1993, *ApJS*, 88, 253
- Theureau, G., Bottinelli, L., Coudreau-Durand, N., Gouguenheim, L., Hallet, N., Loulergue, M., Paturel, G., & Teerikorpi, P. 1998, *A&AS*, 130, 333
- Tripp, T. M., Lu, L., & Savage, B. D. 1998, *ApJ*, 508, 200
- Tripp, T. M., & Savage, B. D. 2000, *ApJ*, 542, 42
- Tripp, T. M., Sembach, K. R., & Savage, B. D. 1993, *ApJ*, 415, 652
- Wakker, B. P., Savage, B. D., Sembach, K. R., Richter, P., Meade, M., & Jenkins, E. B. 2003, *ApJS*, 146, 1
- Wakker, B. P., & van Woerden, H. 1991, *A&A*, 250, 509
- . 1997, *ARA&A*, 35, 217
- Wakker, B. P., et al. 1999, *Nature*, 402, 388
- Weymann, R. J., Morris, S. L., Gray, M. E., & Hutchings, J. B. 1997, *ApJ*, 483, 717
- Zheng, W., et al. 2001, *ApJ*, 562, 152

---

This 2-column preprint was prepared with the AAS L<sup>A</sup>T<sub>E</sub>X macros v5.2.